Journal of Materials Chemistry A

REVIEW

View Article Online
View Journal | View Issue

Cite this: J. Mater. Chem. A, 2023, 11, 15074

Recent progress and prospects in active anion-bearing C12A7-mediated chemical reactions

Xiangyu Zhang,†[a] Zichuang Li,[a] Miao Xu,†[b] Hideo Hosono[c] and Tian-Nan Ye *[a]

Received 24th April 2023
Accepted 2nd June 2023

DOI: 10.1039/d3ta02422a

rsc.li/materials-a

Porous materials have received considerable attention because their unique porous or cage structures can trap different kinds of active species, allowing for unparalleled potential in chemical transformation. As a new type of nanoporous material, $12CaO \cdot 7Al_2O_3$ (C12A7) features a positively charged framework that comprises 3D-connected nanocage structures with an inner diameter of 0.4 nm. A diversity of anions can be easily incorporated into the nanocage structures, endowing C12A7 with various novel physical and chemical properties. In this study, we exhaustively summarize the recent advances in active anions embedded in C12A7 as catalysts or reagents for multiple chemical reactions. Moreover, the diverse routes for the preparation of active species, such as electrons, anions, and radicals, trapped in the cages of C12A7 are itemized elaborately. The roles of the incorporated anions in C12A7 are discussed in depth for chemical transformation. Finally, a perspective on the challenges and developments for future research on active anion-bearing C12A7 materials is proposed. This review provides basic guidance for the rational design and construction of high-performance C12A7-based materials in various applications, especially heterogeneous catalysis.

1. Introduction

Porous materials have attracted great attention over the last two decades owing to their technological applications in many fields.[1] They are generally used as catalysts,[2] adsorbents,[3] and biomaterials[4] owing to their ordered structure arrangement and multiscale pore size distribution. According to the International Union of Pure and Applied Chemistry (IUPAC) definition, porous materials can be classified into three categories based on their pore size distribution: microporous, mesoporous, and macroporous. Compared with mesoporous and macroporous, microporous materials often possess interconnected pores of less than 2 nm in size with large surface areas of 300–2000 $m^2 g^{-1}$. Typically, zeolites,[5] metal organic frameworks (MOFs),[6] and carbon[7] are the most well-known group of microporous materials, in which the unique microporous or cage structure can trap different kinds of molecules and ions. The trapped chemical species enable selective chemical reactions on the surface of the pores, which are believed to be catalytic active sites. When the pore size is reduced to extremely small, the encaged species can be regarded as a quantum dot with the emergence of a quantum effect.[8] Thus, various novel functions are expected to be achieved over microporous materials owing to the low-dimensional nature of their caged state.

$12CaO \cdot 7Al_2O_3$ (C12A7) is a new type of nanoporous material in which the nanoporous framework is positively charged, and thus anions and/or electrons can be encapsulated therein.[9] This nanoporous material differs completely from traditional microporous materials in which positively charged or neutral species are entrapped in the porous structures. In other words,

[a]Frontiers Science Center for Transformative Molecules, School of Chemistry and Chemical Engineering, Shanghai Jiao Tong University, Shanghai 200240, China. E-mail: ytn2011@sjtu.edu.cn

[b]State Key Laboratory of Space Power-sources Technology, Shanghai Institute of Space Power-Sources, Shanghai 200245, China

[c]MDX Research Center for Element Strategy, International Research Frontiers Initiative, Tokyo Institute of Technology, 4259 Nagatsuta, Midori-ku, Yokohama 226-8503, Japan

† Xiangyu Zhang, Zichuang Li and Miao Xu contributed equally to this work.

Dr. Tian-Nan Ye received his PhD degree from Shanghai Jiao Tong University. After that, he joined the Materials Research Center for Element Strategy and worked as a specially appointed assistant professor. During this period, he also received JSPS postdoctoral fellowship and became a JSPS Fellow Researcher at Tokyo Institute of Technology. He is currently an associate professor at the Frontiers Science Center for Transformative Molecules of Shanghai Jiao Tong University. His research interests involve the development of inorganic functional materials and their applications in the catalysis and energy fields.

C12A7 has unique features among porous materials: a positively charged framework comprises 12 sub-nano-cages that are closely packed and share common planes as openings. Because the size of the positively charged cage is comparable to those of the conventional anions, various anions, such as e^-,[10] O_2^-,[11] O^-,[12] H^-,[13] OH^-,[14] NH^{2-},[15] S^{2-},[16] Au^-,[17] F^-,[18] Cl^-,[19] and CN^-,[20] can be easily entrapped therein, as shown in Scheme 1. The exchangeability of the incorporated anions thus provides a convenient means of fine-tuning the selectivity of C12A7.

Because the crystal structure of C12A7 comprises three dimensionally connected sub-nano-cages with an open mouth of the cage at the surface, the substituted anions possibly interacted with each other or transferred to the surface through a monolayered oxide cage wall.[9] These behaviors of the entrapped anions result in various novel properties, including ionic conductivity,[21–24] electron conductivity[10,25] and superconductivity.[26–29] Accordingly, various physical and electronic device applications are achieved, including ionic conductors, cold electron emitters[30–33] and anion emissions.[18,19,34] For example, as the strongest oxidant among active oxygen species, the O^- ion can be extracted from the cage into an external vacuum by applying an electric field with thermal assistance, generating a high-density O^- beam in the order of μA cm^{-2}.[34] The introduction of functional anions in the matrix of C12A7 undoubtedly significantly improved its performance and expanded its applications.

Recently, the increase in publications on C12A7 as heterogeneous catalysis suggests that the field of C12A7-mediated chemical transformations is emerging and will establish a new area of research owing to their high activity associated with structural properties. In this review, we summarize the research progress on active anion-bearing C12A7-mediated chemical reactions in the last two decades and attempt to introduce some common practices in catalyst design. A brief introduction to the preparation methods for various active anions embedded in C12A7 is first introduced in each section. Then, we discuss the functions of the embedded anions in the chemical reactions and systematically explain the relationship between the material structure and the chemical properties of C12A7. Finally, a brief discussion is described on the further challenges and perspectives of C12A7 materials as well as its potential applications in the future.

2. Active ions substituted in C12A7 and its chemical applications

Since the discovery of the first air and room temperature stable electride $[Ca_{24}Al_{28}O_{64}]^{4+}(e^-)_4$ (C12A7:e^-) in 2003,[10] the research interest in $[Ca_{24}Al_{28}O_{64}]^{4+}(X^-)_4$ has increased rapidly, especially focusing on the functional application in chemical transformations. In the last two decades, different active anions (X = e^-,[10] O^-,[12] O_2^-,[11] H^-,[35] Au^-[17] and Pt[36]) embedded in C12A7 have been widely reported in a series of significant chemical reactions, including ammonia synthesis/decomposition, CO_2 reduction/CO oxidation, chemoselective reduction/oxidation and heterolytic hydrogen activation (Scheme 2).

2.1. Electron-substituted C12A7

In C12A7, an extreme case is the total replacement of free O^{2-} ions with anionic electrons, forming the conductive electride material C12A7:e^-.[10] The most characteristic feature of the C12A7:e^- electride is its low work function (2.4 eV),[37]

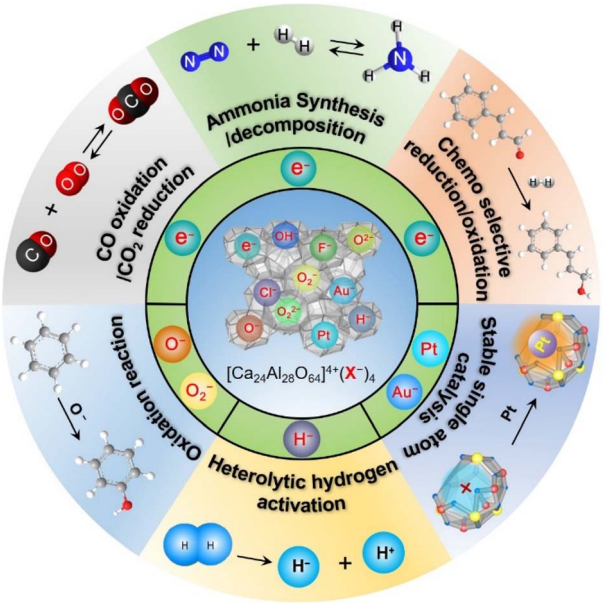

Scheme 2 Various active ions substituted in C12A7 correspond to different chemical applications.

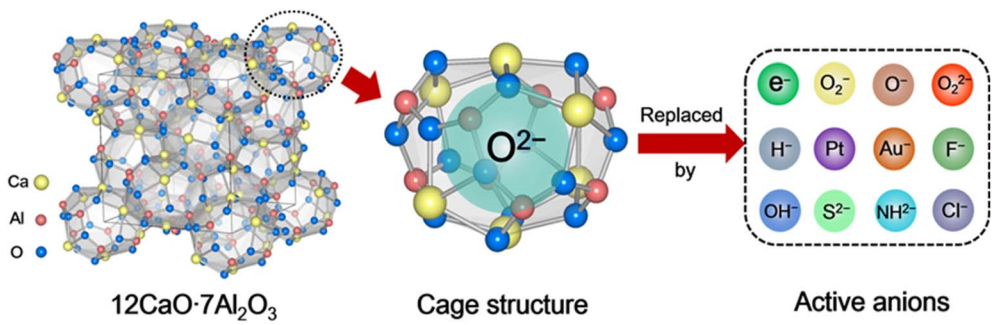

Scheme 1 Structures of C12A7 and single cage structure and exchangeable active anions.

comparable to that of alkali metals, but with higher chemical inertness, which makes this material a promising electron donor in chemical reactions. In this section, we first introduce the preparation methods of C12A7:e^- and then discuss their functional applications.

2.1.1 Preparation method. As shown in Table 1, the preparation method of C12A7:e^- can be mainly divided into physical and chemical processes, and chemical processes include reduction and solid-state reactions. Physical processes and reduction reactions are the processes of removing the free ions (H^- or O^{2-}) of C12A7 by high-energy irradiation or a strong reducing agent to obtain C12A7:e^-. The solid-state reaction is a process of direct synthesis of C12A7:e^- from raw powder material.

In 2002, Hayashi *et al.* reported that the irradiation of hydride ions (H^-) incorporated in C12A7:H^- with ultraviolet light results in a conductive state that persists after irradiation ceases.[38] The photo-activated C12A7:H^- exhibits moderate electrical conductivity (~0.3 S cm^{-1}) at room temperature. The proposed transformation process can be expressed as follows: H^- (cage) → e^- (cage) + H^0 (cage). The positively charged cage electrostatically captures the photo-ionized electron and forms an F^+-like center. The electron concentration (N_e) determined by EPR (electron paramagnetic resonance) was 2×10^{19} cm^{-3}. Because the electron is weakly bound in the cage, the wave-function spreads spatially. Consequently, electrons could migrate throughout the framework by variable-range hopping.

The reduction in C12A7 is also achieved by ion implantation, one of the non-equilibrium physical processes in which a high concentration of ions can be introduced in a designated small area with excellent controllability. It is widely used for the modification of thin film materials. Miyakawa *et al.* conducted Ar^+ ion implantation in polycrystalline C12A7 thin films and found that the free O^{2-} ions could be removed from the cage by the collision of O^{2-} ions and Ar^+ ions, thus leaving free e^- therein.[39] The produced electrons by Ar^+-implantation could be expressed using the following equation: O^{2-} (cage) → $2e^-$ (cage) + $1/2O_2$ (gas). Using this method, the N_e of the final obtained C12A7:e^- can reach ~1.4×10^{21} cm^{-3}. It is noteworthy that ion implantation technology enables a higher N_e than that of UV irradiation with a designated narrow space.

Compared with physical processes, the types of C12A7 reduction reactions are more abundant in chemical processes. In 2003, Matsuishi *et al.* removed ~100% of clathrated O^{2-} ions from C12A7 by the thermal treatment of C12A7 singe crystal under Ca metal vapor.[10] Single crystal C12A7 and Ca metal are sealed in a vacuum silica glass tube (~10^{-3} torr) and treated at 700 °C (Fig. 1a). The heating process ensures that Ca metal volatilizes into vapor and reacts with the free O^{2-} ions of C12A7 to form CaO, which was subsequently removed by mechanical polishing. The formation mechanism for the C12A7:e^- can be expressed as follows: O^{2-} (cage) + Ca → $2e^-$ (cage) + CaO. With the extension of the Ca vapor treatment time, the color of the sample changes from transparent to green and, finally, to black with the N_e reaching up to 2×10^{21} cm^{-3} (Fig. 1b). It is noteworthy that the Ca treatment requires a long duration (240 hours for a 0.4 mm thin single crystal) to extract the total free O^{2-} ions because the heating temperature is limited to 700 °C at maximum, preventing the reaction of C12A7 crystal and Ca to form $Ca_3Al_2O_6$ (C3A). The surface generation of dense CaO film also hinders the deep reduction of bulk C12A7. Further, the replacement of free O^{2-} ions is incomplete owing to the formation of a surface CaO layer that acts as a diffusion barrier.

The above drawbacks were overcome by employing Ti metal vapor treatment. Ti could form stable nonstoichiometric oxides over a wide chemical composition range ($1 < x < 2$ in TiO_{2-x}), and these Ti sub-oxides exhibit metallic conductivity. The outward diffusion of free O^{2-} ions of C12A7 cannot be blocked

Table 1 Summary of C12A7:e^- electride preparation processes

Process		Precursor	Reacting process	N_e (cm^{-3})
Physical process	UV illumination[38]	Single crystal	H^- (cage) → e^- (cage) + H^0 (cage)	2×10^{19}
	Ion implantation[39]	Thin film	O^{2-} (cage) → $2e^-$ (cage) + $1/2O_2$ (gas)	1.4×10^{21}
Chemical process (reduction reaction)	Ca vapor treatment[10]	Single crystal	O^{2-} (cage) + Ca → $2e^-$ (cage) + CaO	2.3×10^{21}
	Ti vapor treatment[25]	Single crystal	O^{2-} (cage) + Ti → $2e^-$ (cage) + TiO_{2-x}	2.3×10^{21}
	CO gas[40]	Single crystal/powder/thin film	O^{2-} (cage) + CO → $2e^-$ (cage) + CO_2	8×10^{19}
	Melt solidification	No specific one	C_2^{2-} (cage) → $2e^-$ (cage) + 2C or C_2^{2-} (cage) + $2O^{2-}$ → $6e^-$ (cage) + 2CO	9×10^{19}
	Glass-ceramics[41]	No specific one		9×10^{19}

Process	Reactant	Reaction condition	N_e (cm^{-3})
Chemical process (solid–state reaction)	C12A7, CA, Ca shot[42]	Sealed in vacuum	2.3×10^{21}
	CaO, Al_2O_3, Al[43]	Ar atmosphere	1.2×10^{21}
	CaO, Ca, Al_2O_3[44]	Spark plasma sintering	2.1×10^{21}
	$C_{12}H_{10}Ca_3O_{14} \cdot 4H_2O$, Al_2O_3[45]	Spark plasma sintering	2.0×10^{21}

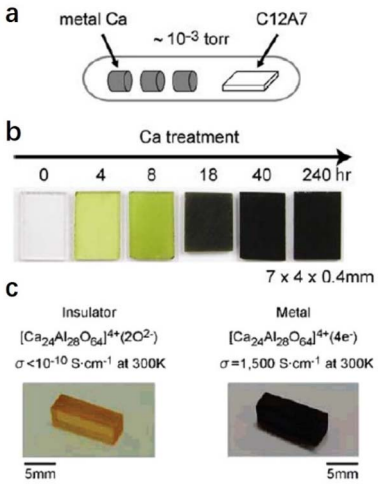

Fig. 1 (a) Schematic illustration of the synthesis process for C12A7 electride *via* Ca treatment. (b) The Ca treatment changes the sample color from colorless to green and, finally, to black, with increasing duration of the Ca treatment. Copyright 2007, Springer Nature. (c) The Ti treatment changes the sample color from orange to black. The orange colour comes from Ir^{4+} dissolved from the Ir crucible used for single crystal growth.[46] Copyright 2007, American Chemical Society.

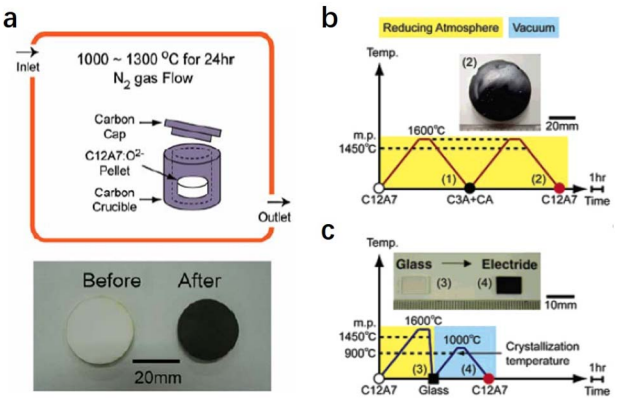

Fig. 2 Synthesis processes for C12A7 electride under a reducing atmosphere. (a) Schematic illustration of CO/CO_2 reduction treatment and image of the obtained dark green electride disk. Copyright 2007, Springer Nature. Melt-solidification (b) and glass-ceramic (c) processes. Copyright 2005, American Chemical Society.

even if a thick titanium oxide layer completely covers the sample surface. Additionally, high temperatures up to ~1300 °C can be used for the calcination reduction process because Ti metal does not react with C12A7 up to this temperature. Kim *et al.* reported the treatment of C12A7 single crystals by Ti metal vapor at ~1100 °C.[25] The change in color from transparent orange tint to black indicates an increased electron concentration and enhanced electrical conductivity (Fig. 1c). Owing to the high reaction temperature, the diffusion rate of O^{2-} in C12A7 increases by several orders of magnitude, resulting in the effective shortening of the heating time. Accordingly, N_e reaches the theoretical maximum value of $\sim 2.3 \times 10^{21}$ cm^{-3}.

In addition to Ca and Ti metal vapor, the treatment of C12A7 in reducing atmospheres of CO/CO_2 has also been investigated. Kim *et al.* placed a C12A7 sample in a carbon crucible with a cap heated at 1000–1300 °C for 24 h in a flowing N_2 atmosphere (Fig. 2a).[40] The atmosphere inside the carbon crucible during the treatment is strongly reductive CO/CO_2 with a pO_2 of 10^{-19}–10^{-17} atm. Under this condition, CO gas reacts with free O^{2-} ions of C12A7 to generate CO_2, and then the electrons are injected into the cages to compensate for the positively charged lattice framework. The reduction process can be expressed as the following equation: O^{2-} (cage) + CO (gas) → $2e^-$ (cage) + CO_2 (gas). The color of the sample becomes dark green because of the relatively low N_e of 8×10^{19} cm^{-3}. Unlike metal vapour treatment, which inevitably produces the metal oxide layer at the surface, the sample surface remains clean without forming any additional impurities during the reaction. Hence, this reduction strategy can be applied to C12A7 with different sample forms (single crystals, powder and thin films).

A simple and efficient synthesis method of C12A7:e^- is vital for practical applications. Kim *et al.* reported facile preparation of C12A7:e^- electride from its melting and glass states in a carbon crucible with a carbon cap at 1600 °C (Fig. 2b and c).[41] This high temperature produces a strongly reducing atmosphere inside the crucible with partial oxygen pressure as low as 10^{-16} atm. It is found that C_2^{2-} ions dissolved into the melt from the carbon crucible to compensate for the oxygen deficiency arising from the strongly reducing atmosphere. Because of the similar anion sizes of C_2^{2-} (1.2 Å) and O^{2-} (1.4 Å), the C_2^{2-} anion can operate as a template under a reducing atmosphere. The possible reaction mechanism can be expressed as follows: C_2^{2-} (melt or glass) → C_2^{2-} (cage) + O^{2-} (cage) → $4e^-$ (cage) + 2C or C_2^{2-} (cage) + $2O^{2-}$ (cage) → $6e^-$ (cage) + 2CO (gas). The resultant crystallized C12A7:e^- is dark green, which suggests a mediate electronic conductivity and that the N_e can reach 9×10^{19} cm^{-3}.

The metal–insulator transition of $[Ca_{24}Al_{28}O_{64}]^{4+}(O^{2-})_{2-x}(e^-)_{2x}$ occurs at $N_e \approx 1 \times 10^{21}$ cm^{-3}, which is the prerequisite for the high electron donation ability of C12A7:e^-. Matsuishi *et al.* reported a direct synthesis method for the preparation of C12A7:e^- powder with an electron density up to a theoretical maximum of 2.33×10^{21} cm^{-3}.[42] C12A7:e^- powder was synthesized by a reaction of C12A7, $CaO \cdot Al_2O_3$ (CA), and Ca metal at 700–1100 °C: $0.8Ca_{12}Al_{14}O_{33} + 1.4CaAl_2O_4 + Ca \rightarrow 1/2[Ca_{24}Al_{28}O_{64}]^{4+}(e^-)_4$. This process comprises the following seven-step procedure. First, a mixture of C12A7 and CA was prepared by a reaction of $CaCO_3$ and γ-Al_2O_3 with a molar ratio of 11 : 7 at 1300 °C in ambient air: $11CaCO_3 + 7Al_2O_3 \rightarrow 0.8Ca_{12}Al_{14}O_{33} + 1.4CaAl_2O_4 + 11CO_2\uparrow$(i). The sintered mixture (C12A7 + CA) was ball-milled (ii), and subsequently degassed at 700 °C for 2 h in the air (iii). After that, the mixture was heated at 1100 °C for 15 h in a dynamically evacuated silica tube (~1×10^{-4} Pa) (iv). The C12A7 + CA and Ca metal shots were sealed in an evacuated silica tube and heated at 700 °C for 15 h (v). The tube was then opened in an Ar-filled groove box, and the obtained material was ground to spread Ca within the mixture (vi). Finally, the mixture was squeezed into a single-ended silica tube, which was subsequently evacuated

and sealed. The tube was sealed in another evacuated silica tube. The doubly sealed tube was then heated at 1100 °C for 2 h (vii). This method involves multiple steps, such as crystallization of the mixture precursor of C12A7 and CA, strict evacuation, and encapsulation.

Jiang *et al.* reported a facile one-step and scalable aluminothermic synthesis method of C12A7:e^- with N_e up to 1.23×10^{21} cm^{-3} (Fig. 3a).[43] A mixture of CaO, Al_2O_3, and Al powders with molar ratios of $12:7(1-x):14(x)$ and $x = 0$–25% was placed in an alumina crucible with an alumina plate cover. Next, it was calcined in a horizontal tube furnace at 1000–1300 °C for 8 h in a flowing Ar atmosphere. After that, Li *et al.* reported another direct and efficient route to fabricate C12A7:e^- from the raw materials of CaO, Al_2O_3 and Ca powders (Fig. 3b).[44] The powders of CaO, Al_2O_3 and Ca with mole ratios of $(12-x):7:x$ with $x = 0$–1.6 were mixed by a mechanical ball mill under an inert atmosphere. The mixed powders were placed into a ceramic die and sintered at 1000–1200 °C for 20 minutes in a 10^{-2} Pa vacuum under a uniaxial pressure of 60 MPa using the SPS system, and the N_e of the obtained C12A7:e^- reaches 2×10^{21} cm^{-3}. Moreover, Xiao *et al.* mixed stoichiometric $C_{12}H_{10}Ca_3O_{14}$ (calcium citrate) and Al_2O_3 powder into a graphite mold and then placed it into an SPS sintering system at 1000 °C for 5 minutes. A self-reduction process is achieved by *in situ* formed CO gas inside the graphite mold, avoiding the generation of impurities and simplifying the synthesis process. The N_e of the obtained C12A7:e^- reaches 2×10^{21} cm^{-3}.[45]

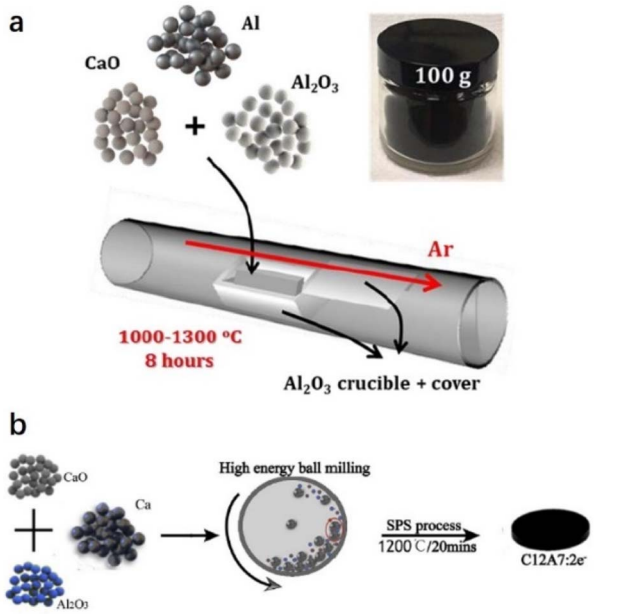

Fig. 3 (a) Schematic of aluminothermic synthesis of C12A7:e^- *via* one-step calcination of mixtures of oxide and Al. Inset is an image of 100 g mass-produced C12A7:e^- powders. Copyright 2019, American Chemical Society. (b) Schematic of the synthesis process of C12A7:e^- *via* SPS of mixtures of oxide and Ca. Copyright 2019, Elsevier.

2.1.2 Electron donor for catalysis

2.1.2.1 Ammonia synthesis/decomposition. Ammonia synthesis from N_2 and H_2 is regarded as one of the most important catalytic reactions because NH_3 is widely used for the production of synthetic fertilizers and chemical raw materials in the industry. Owing to the extremely large bond energy of N≡N bond, industrial ammonia synthesis of the Haber–Bosch process with iron-based catalysts requires high temperature (673–873 K) and high pressure (20–40 MPa).[47] For transition metal catalysts, N_2 is fixed to the metal through σ bond donation, and then adsorbed N_2 also accepts electrons to its antibonding orbitals by π backdonation. This electron acceptance process can be enhanced by electron donors, which promotes the weakening of the N≡N bond.

C12A7:e^- comprises 3-dimensionally (3D) connected sub-nanometer-sized cages, in which anionic electrons are incorporated as counter anions. The 3D connection of these cages forms unique bands below the cage wall conduction band, called the cage conduction band (CCB).[48] Because electrons are

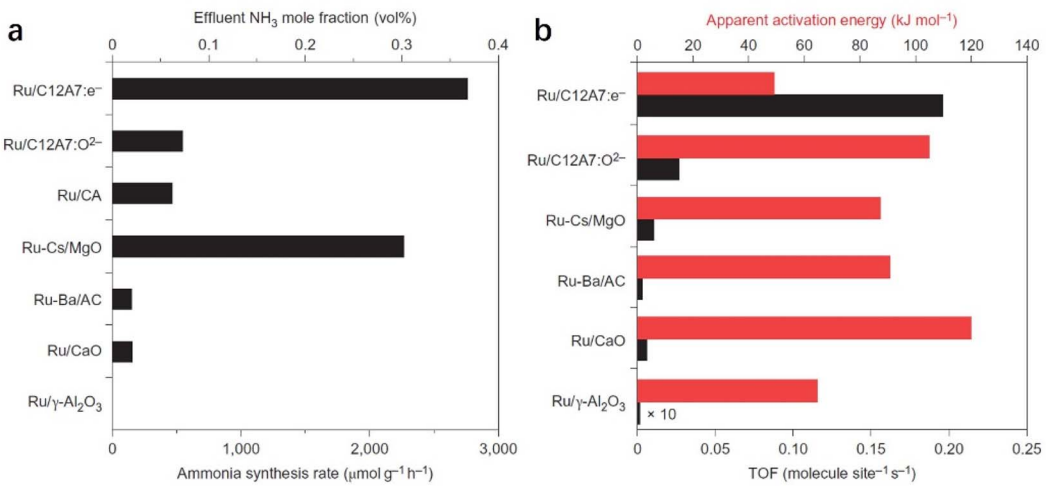

Fig. 4 (a) Catalytic performance for NH_3 synthesis over various Ru (1 wt%)-loaded catalysts at 400 °C and 0.1 MPa. (b) TOFs and apparent activation energies of various Ru (1 wt%)-loaded catalysts for ammonia synthesis. Copyright 2012, Springer Nature.

injected into this CCB, a low work function property emerges for C12A7:e$^-$ material.[37] In this context, Kitano *et al.* reported that the C12A7:e$^-$ electride operates as an excellent electron donor to promote transition metal Ru in catalytic ammonia synthesis.[49] Although the specific surface area of C12A7:e$^-$ is as low as 1–2 $m^2\ g^{-1}$, Ru-loaded C12A7:e$^-$ catalysts exhibit a high NH_3 synthesis rate of 8.2 mmol $g^{-1}\ h^{-1}$, which is close to that of the bench-marked catalyst of Cs–Ru/MgO (Fig. 4a). Compared with other Ru-based catalysts, the extremely high turnover frequency (TOF) and relatively small activation energy indicate that C12A7:e$^-$ greatly contributed to promoting Ru metal for ammonia synthesis (Fig. 4b).

Because the catalytic performance of Ru/C12A7:e$^-$ strongly depends on the electron donation ability that stems from the unique electronic properties of C12A7:e$^-$, Kanbara *et al.* prepared a series of C12A7:e$^-$ powders with controlled electron concentrations (N_e). The color of the samples was changed from white to green and black as N_e increased from 0 to 2.0×10^{21}

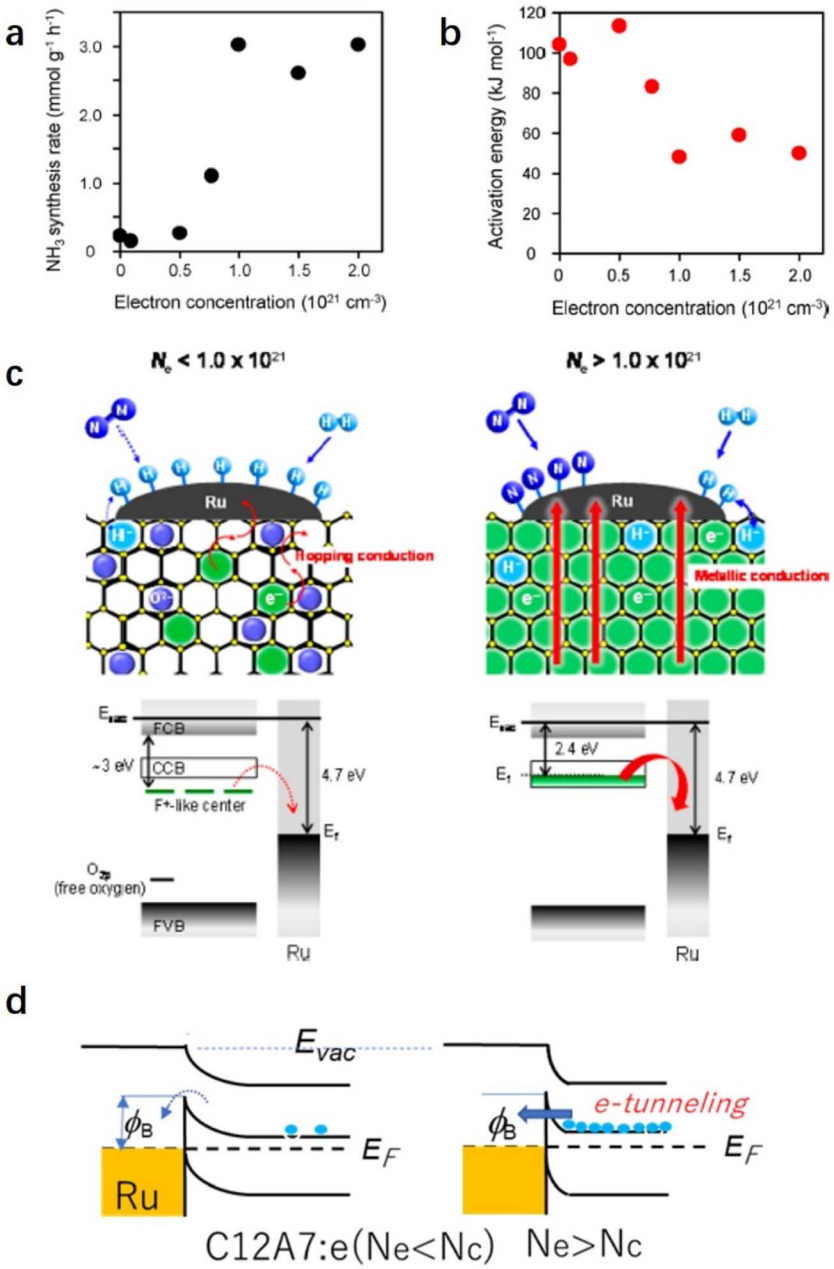

Fig. 5 (a) Ammonia synthesis rate and (b) activation energy with Ru/C12A7:e$^-$ catalysts as a function of electron concentration. (c) Proposed reaction mechanism for ammonia synthesis over Ru/C12A7:e$^-$. Copyright 2015, American Chemical Society. (d) Energy barrier at Ru/C12A7:e$^-$ interface. Because the work function (ϕ) of Ru is much higher than that of C12A7:e$^-$, the contact with a Schottky barrier and a height of Δ_ϕ is formed. When N_e is higher than N_c (critical concertation for metal–insulator transition), electrons can pass through this barrier by tunneling.[51] Copyright 2021, Springer Nature.

cm^{-3}. The reaction rate of ammonia synthesis over Ru/C12A7:e^- obviously increased with N_e above 0.5×10^{21} cm^{-3} and reached a plateau at 1.0×10^{21} cm^{-3} (Fig. 5a).[50] Interestingly, the correlation of the apparent activation energies (E_a) with N_e has a similar trend to the relationship between the ammonia formation rate and N_e, in which E_a of Ru/C12A7:e^- with N_e above 1.0×10^{21} cm^{-3} is almost half that of the catalyst with N_e below 0.5×10^{21} cm^{-3} (Fig. 5b). The electronic structure of C12A7 with and without electrons is depicted in Fig. 5c. Under low N_e condition, the electron transfer from C12A7:e^- to transition metal became difficult owing to the presence of an interfacial Schottky barrier, resulting in an inferior catalytic performance with significantly elevated E_a. The metal–insulator transition of C12A7:e^- occurred at approximately 1.0×10^{21} cm^{-3}, and the C12A7:e^- with high N_e (2.3×10^{21} cm^{-3}) showed high conductivity (1500 S cm^{-1})[25] and low work function (2.4 eV).[37] Accordingly, smooth electron injection occurs from C12A7:e^- to Ru, which accounts for the low activation barrier of N_2 dissociation.

The electron-donation capability of C12A7:e^- is experimentally evidenced by Fourier transform infrared (FT-IR) spectra of N_2 adsorption. The vibrational peaks of N_2 adsorption on Ru/C12A7:e^- are observed at lower wavenumbers than those on Ru/C12A7:O^{2-} and Ru/Al_2O_3 (Fig. 6a).[49] This shift implies that the N≡N bond is significantly weakened by the donated electrons from C12A7:e^- to the absorbed N_2, resulting in a significantly suppressed energy barrier of N_2 dissociation compared to other conventional Ru-loaded catalysts. It is also noted that such supported Ru metal is not subject to hydrogen poisoning owing to the hydrogen storage capacity of C12A7:e^-. The C12A7:e^- can capture hydrogen as H^- ions in the cages through the reaction of electrons with the spillover of hydrogen from the Ru surface ($H^0 + e^- \rightarrow H^-$). The electrons are regenerated in the cages by releasing H atoms from the cages: H^- (cage) → H^0 (release from the cage) + e^- (cage). This reversible e^-–H^- exchange reaction in Ru/C12A7:e^- effectively prevents hydrogen poisoning on the Ru surface, which is also confirmed by temperature-programmed absorption (TPA). Ru/CaO·Al_2O_3 without a positively charged nanocage structure cannot absorb hydrogen, while Ru/C12A7:O^{2-} and Ru/C12A7:e^- store hydrogen at 350–600 °C, and the hydrogen storage ability of Ru/C12A7:e^- is about 4 times higher compared to that of Ru/C12A7:O^{2-} (Fig. 6b).[52] Temperature-programmed desorption of H_2 (H_2-TPD) of these catalysts after ammonia synthesis demonstrates that only Ru/C12A7:e^- shows a clear peak for H_2 desorption at 300–500 °C (Fig. 6c), which indicates reversible e^-–H^- exchange during ammonia synthesis.

The difference in the reaction mechanism of NH_3 synthesis between Ru/C12A7:e^- and conventional catalysts is illustrated in Fig. 7.[52] In conventional catalysts, N_2 and H_2 molecules are dissociated on the surface of transition metal through a Langmuir–Hinshelwood mechanism, where the energy barrier of N_2 dissociation (E_{dis}) is the highest among all elementary steps. Therefore, the N_2 cleavage is regarded as the rate-determining step (RDS) (Fig. 7a). In contrast, the NH_3 synthesis rate of Ru/C12A7:e^- is not limited by this step because of the enhanced N_2 dissociation on Ru facilitated by electron injection from C12A7:e^-. Accordingly, the RDS shifted from N_2 dissociation to the formation of N–H_n species (Fig. 7b).

The C12A7:e^- support can also boost NH_3 synthesis over the cobalt (Co) catalyst (Fig. 8a).[53] According to the scaling relationship of NH_3 synthesis proposed by Nørskov *et al.*, Co metal is not considered an optimal metal for dissociative N_2 adsorption.[54] Generally, harsh reaction conditions are required for Co-based catalysts in NH_3 synthesis, and the apparent activation energies are often as high as 90–110 kJ mol^{-1}. In contrast, Co/C12A7:e^- promotes the N_2 activation with a low activation energy (*ca.* 50 kJ mol^{-1}) even under relatively mild conditions, which is similar to those of state-of-the art Co catalysts, such as Co_3Mo_3N, LaCoSi, and Co–LiH (40–60 kJ mol^{-1}). As shown in Fig. 8b, the activity of Co/MgO is unsatisfactory despite the addition of the Cs promoter. In sharp contrast to other oxide support materials, Co(2.6 wt%)/C12A7:e^- exhibits high catalytic activity, and the reaction rate is an order of magnitude higher than the other Co catalysts. The initial temperature for NH_3 generation over Co/C12A7:e^- is ~200 °C lower than that for the Co/C12A7:O^{2-} catalyst. The high performance of the Co/C12A7:e^- catalyst is attributed to the electron donation power of C12A7:e^- with a low WF (2.4 eV), which enables N_2 cleavage at Co metal at low temperatures. This study again emphasizes that

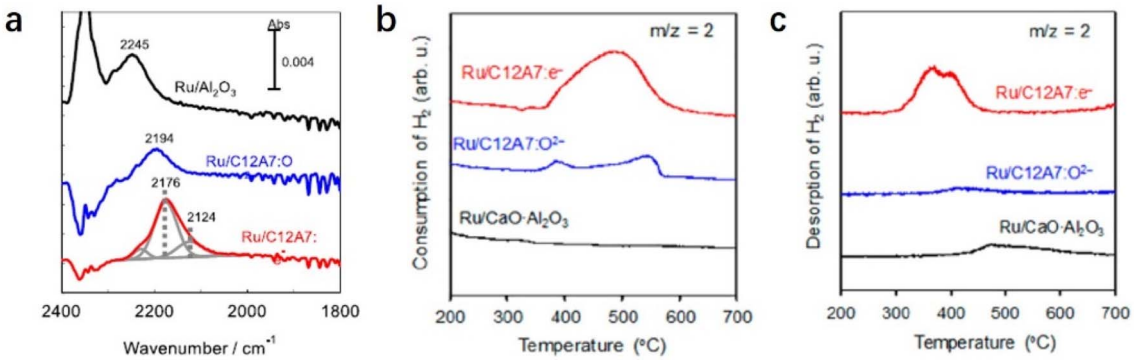

Fig. 6 (a) Difference FT-IR spectra of N_2 adsorbed on Ru/Al_2O_3, Ru/C12A7:O^{2-}, and Ru/C12A7:e^- at −170 °C. Copyright 2012, Springer Nature. (b) H_2-TPA and (c) Ar-TPD profiles of Ru/CaO·Al_2O_3, Ru/C12A7:O^{2-}, and Ru/C12A7:e^-. Copyright 2015, Springer Nature.

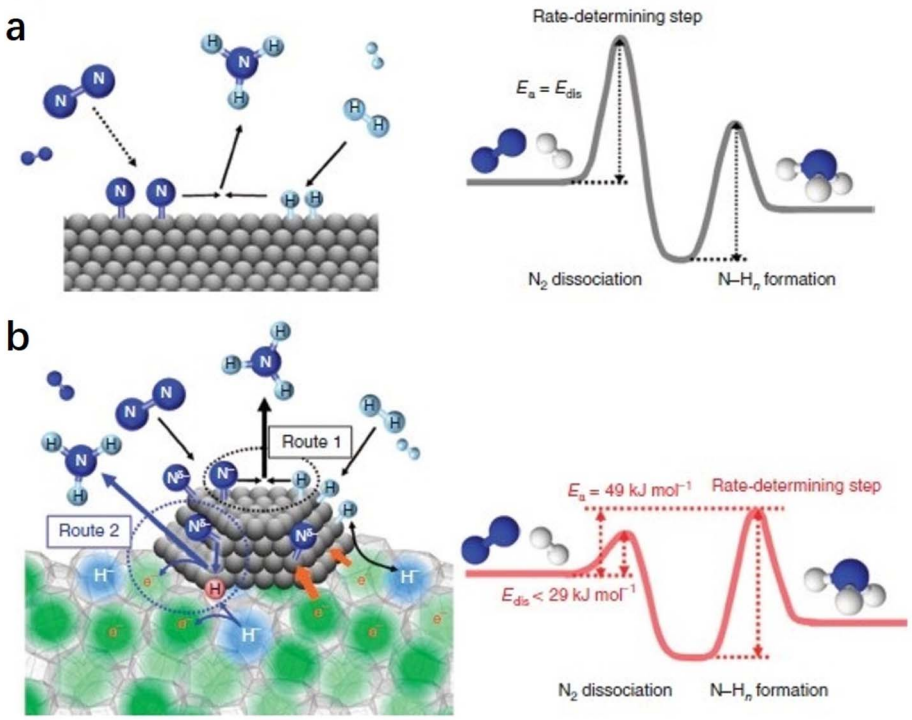

Fig. 7 Reaction mechanism and energy diagram for NH_3 synthesis on (a) conventional catalyst and (b) Ru/C12A7:e^- catalyst. Copyright 2015, Springer Nature.

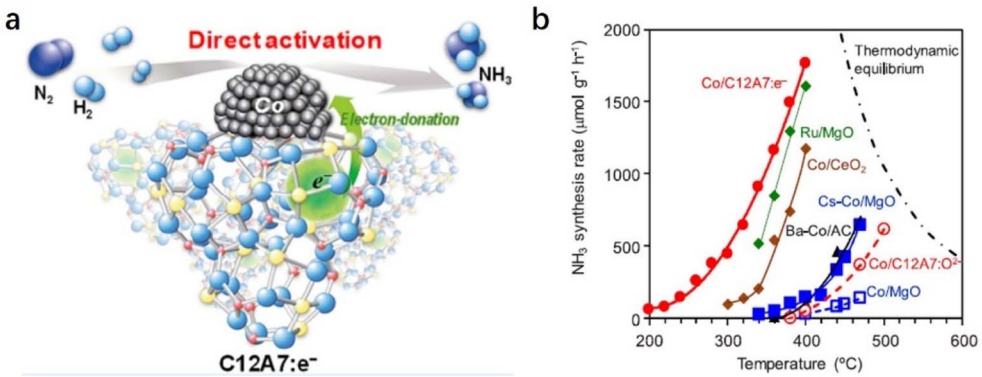

Fig. 8 (a) Reaction mechanism for NH_3 synthesis on Co/C12A7:e^- catalyst. (b) Temperature dependence of NH_3 synthesis rate for the supported Co catalysts. Reaction conditions: WHSV, 18 000 mL g^{-1} h^{-1}; pressure, 0.1 MPa. Copyright 2019, American Chemical Society.

electron injection from C12A7:e^- plays an important role in the promotion of transition metals that catalyze ammonia synthesis.

In the NH_3 decomposition reaction, it is generally accepted that the RDS is the associative desorption of N adatoms from the metal surface. Hayashi *et al.* reported a facile NH_3 decomposition on Ru-loaded C12A7:e^- electride with a low activation energy (Fig. 9).[55] They attributed the high catalytic performance of Ru/C12A7:e^- to the low work function feature of C12A7:e^- electride. On the traditional Ru surface, the 2p-orbital of N interacts with the d-orbital of Ru at the Fermi level (E_F). The anti-bonding orbital (Ru–N* orbital) of the Ru–N bond is far away from E_F (+3 eV), and the bond orbital is about 5.5 eV below E_F. On the Ru/C12A7:e^- surface, driven by the difference in the work function between Ru and C12A7:e^-, the electrons in the CCB state of C12A7:e^- can transfer to Ru, raising the E_F of Ru metal relative to the N 2p orbitals. Consequently, in Ru/C12A7:e^-, the state of the Ru–N* orbital becomes much closer to E_F compared with that of bare Ru metal, enabling a favored electron injection into the Ru–N* orbital (Fig. 9b). Thus, the activation and cleavage of the Ru–N bond is significantly promoted over Ru/C12A7:e^-, achieving efficient NH_3 decomposition under mild conditions.

2.1.2.2 Selective hydrogenation of α, β-unsaturated aldehydes. Chemoselective hydrogenation is a powerful tool for achieving a controlled reduction in various organic compounds. Tuning the electronic structure of metal catalysts, also known as electronic metal–support interactions (EMSI), is considered an efficient strategy to improve catalytic performance.[56] Because of the strong electron donation power of C12A7:e$^-$, the electronic structure of the loaded active metal can be easily manipulated through the role of EMSI, thereby controlling the adsorption and activation of the substrates that determine the overall activity and selectivity.

Our group reported that Ru–Fe alloy nanoparticles deposited on C12A7:e$^-$ electride enabled the highly efficient selective hydrogenation of α,β-unsaturated aldehydes.[57] Ru–Fe alloys are formed on C12A7:e$^-$ surface, and both Fe and Ru are homogeneously distributed in the nanoparticles (Fig. 10a). For the hydrogenation of α,β-unsaturated aldehydes, high selectivity and activity of the unsaturated alcohol product is difficult to achieve because of the thermodynamically favored hydrogenation of the C=C bond. Thus, conventional hydrogenation catalysts of Pt, Pd, and Ru preferentially produce saturated aldehydes. In the C12A7:e$^-$ electride catalyst, the electronic nature of the Ru–Fe nanoparticles can be modified by the electron donation of C12A7:e$^-$, leading to a remarkable increase in the selectivity of unsaturated alcohol. It is noted that the selectivity of unsaturated alcohol increases with the enhanced N_e of C12A7:e$^-$, which suggests that the hydrogenation process strongly depends on the electronic properties of C12A7:e$^-$ support (Fig. 10b). The electron donation capabilities of C12A7:e$^-$ was confirmed by diffuse reflectance infrared Fourier transform (DRIFT) spectroscopy using CO as a probe molecule (Fig. 10c). Compared with the linear Ru^0–CO (2050 cm^{-1}) peak of Ru–Fe/C12A7:O^{2-}, a clear redshift is identified in Ru–Fe/C12A7:e$^-$ (2020 cm^{-1}), implying that the C≡O bond on Ru–Fe/C12A7:e$^-$ is weakened by electrons, which provides evidence for the strong electronic modification of C12A7:e$^-$ electride.

The possible reaction mechanism of the selective hydrogenation process on Ru–Fe/C12A7:e$^-$ is shown in Fig. 10d. The electron-rich Ru–Fe surface repels the C=C bond *via* the repulsive interaction between metal d-orbitals and C=C bonds, favoring a vertical adsorption configuration *via* the C=O bond. Moreover, the Fe site also operates as an electrophilic site, which enables the attraction of the C=O bond *via* the lone electron pair of the oxygen atom, resulting in the weakening of the C=O bond. Therefore, the selective hydrogenation of C=O bonds is preferred even in the presence of C=C bonds.

2.1.2.3 CO oxidation reaction. The investigation of C12A7:e$^-$ as an electron donor is mainly carried out in reductive

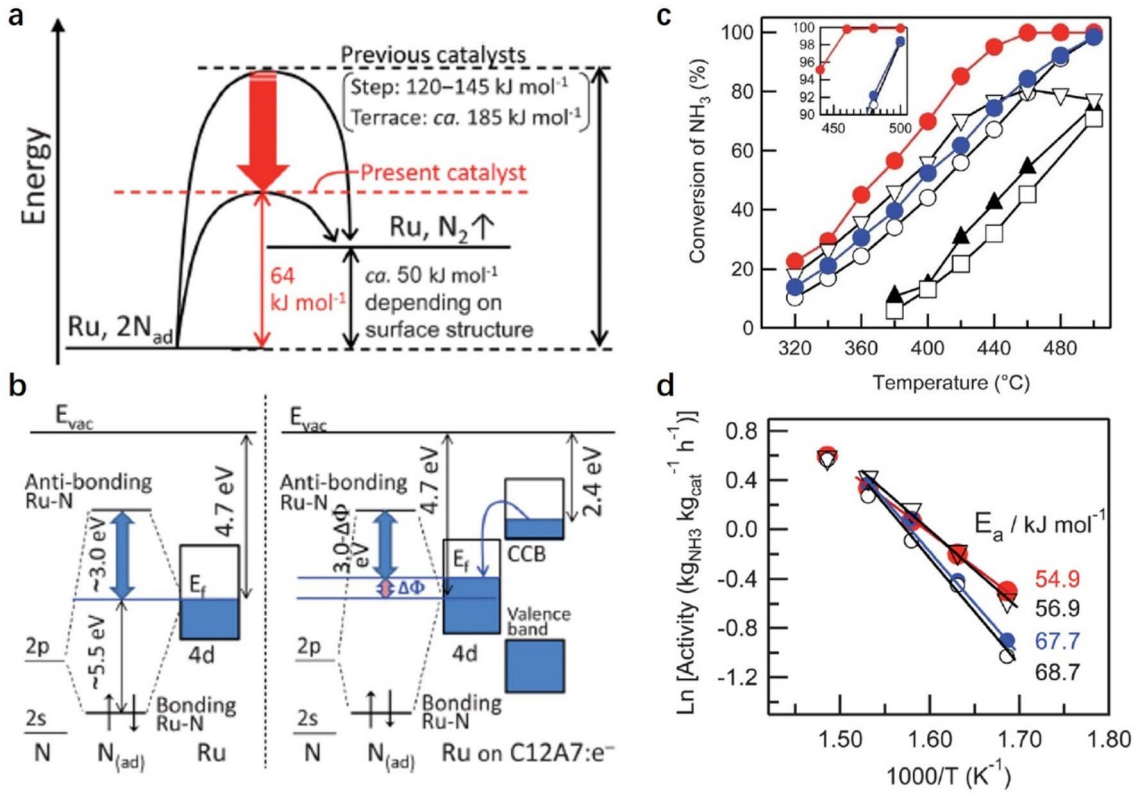

Fig. 9 (a) Energy profiles for dissociative N_2 adsorption and recombinative N_2 desorption on Ru/C12A7:e$^-$ and Ru metals. (b) Schematic diagram showing how the Ru–N bond is weakened on Ru/C12A7:e$^-$. E_f and E_{vac} denote the Fermi and vacuum levels, respectively, where blue shading denotes the electron-filled states. (c) Temperature dependence of NH_3 decomposition activity for various Ru-supported catalysts: red dots, Ru/C12A7:e$^-$; ○, Ru/C12A7:O^{2-}; blue dots, Ru–Cs/MgO; ▲, Ru/CaO; □, Ru/Al_2O_3; and ▽, Ru–K/C. (d) Arrhenius plots of NH_3 decomposition rate over Ru/C12A7:e$^-$ (red dots), Ru/C12A7:O^{2-} (○), Ru–Cs/MgO (blue dots), and Ru–K/C (▽). Copyright 2013, Royal Society of Chemistry.

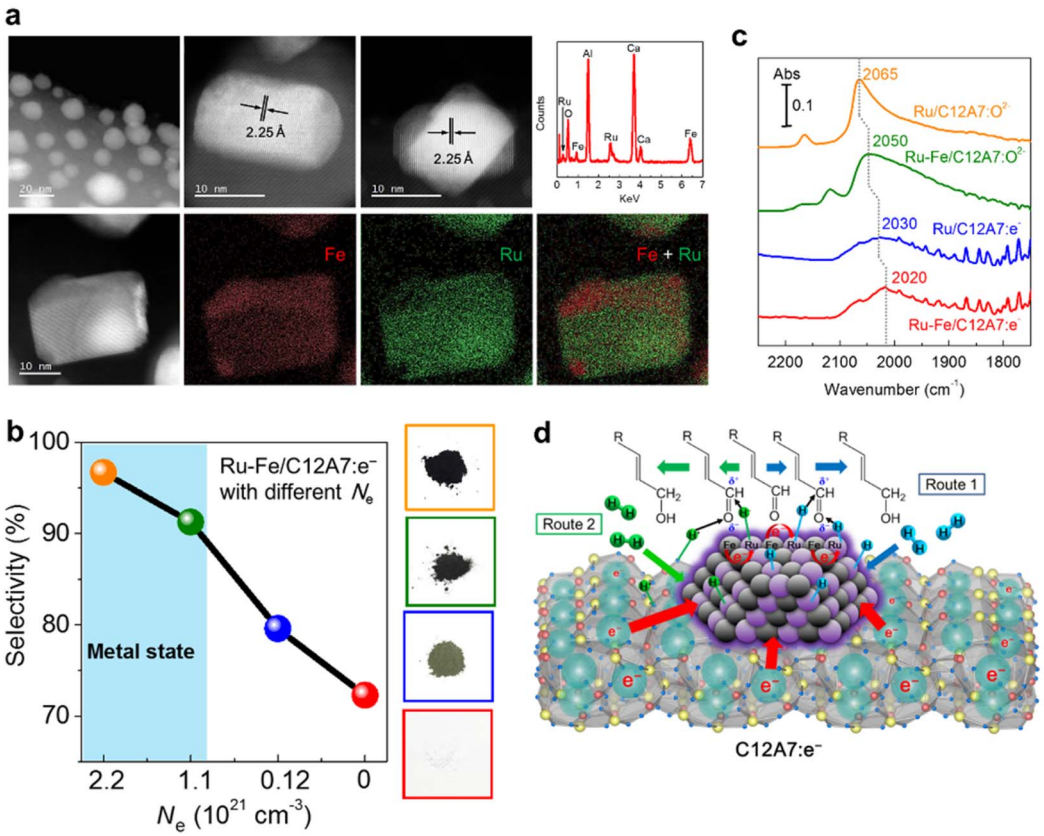

Fig. 10 (a) High-angle annular dark field scanning transmission electron microscopy HAADF-STEM images of Ru–Fe/C12A7:e$^-$. (b) Cinnamaldehyde hydrogenation selectivity with Ru–Fe loaded C12A7:e$^-$/O^{2-} catalysts as a function of electron concentration. (c) Difference DRIFTS spectra for adsorption of CO onto Ru/C12A7:O^{2-}, Ru–Fe/C12A7:O^{2-}, Ru/C12A7:e$^-$, and Ru–Fe/C12A7:e$^-$ at ~170 °C under 5 kPa of CO. (d) The possible pathway for chemoselective hydrogenation of α, β-unsaturated aldehydes over Ru–Fe/C12A7:e$^-$. Copyright 2016, Royal Society of Chemistry.

atmospheres. Interestingly, C12A7:e$^-$ is stable in oxidative atmospheres up to 300 °C, which implies that C12A7:e$^-$ can also function as an electron donor under oxidative atmospheres below 300 °C.[42] Therefore, Ru nanoparticles on C12A7:e$^-$ have higher oxidation resistance than those on conventional oxide supports.[58] As expected, C12A7:e$^-$ supported Ru catalysts exhibited high and stable catalytic activity for CO oxidation reaction.[59] It is generally accepted that O_2 molecules are adsorbed on the support, such as Au/TiO_2, and then the reaction proceeds through the lattice oxygen-mediated Mars–van Krevelen (MvK) mechanism.[60] Additionally, CO oxidation can be promoted by the EMSI of the metal–support interface of the reducible oxide-supported metal catalysts.[61]

The CO oxidation reaction over Ru/C12A7:e$^-$ is initiated at ~70 °C, which is obviously lower than that of Ru/C12A7:O^{2-} (Fig. 11a).[59] Ru/C12A7:e$^-$ shows similar catalytic activity to Ru/TiO_2 but with much-suppressed activation energy (E_a) (Fig. 11b), and the CO conversion reached 100% at around 140 °C, even though with a smaller surface area of Ru/C12A7:e$^-$ (~1 m^2 g−1) compared with Ru/TiO_2 (54 m^2 g^{-1}). The high catalytic performance of Ru/C12A7:e$^-$ is mainly attributed to the high electron donation power of the C12A7:e$^-$ support. As shown in Fig. 11c, reducible oxides, such as TiO_2, rather than nonreducible supports (*e.g.*, Al_2O_3), facilitate CO oxidation over the active transition metal, in which lattice oxygen near the metal is also involved in the formation of CO_2 and is subsequently recovered by gas-phase O_2 (MvK mechanism).[60]

However, CO oxidation over Ru/C12A7:e$^-$ does not proceed through the MvK mechanism because the framework oxygens are difficult to remove below 700 °C.[10] As shown in Fig. 11d, CO and O_2 molecules are adsorbed on the Ru surface, and O_2 is immediately cleaved into oxygen adatoms. The rate-determining step of CO oxidation over Ru catalysts is well accepted as the formation of the CO–O bond.[62] In C12A7:e$^-$ catalyst, the energy barrier of this step is significantly suppressed by the electride character as follows: the anionic electrons are injected from C12A7:e$^-$ to Ru, enabling the charge transfer from Ru d-orbitals to the 2π* antibonding orbitals of CO. Consequently, the C–O bond is weakened with the formation of $C^{\delta+}$–$O^{\delta-}$ species. The electronic interaction between C12A7:e$^-$ and Ru also favors the generation of negatively charged O adatoms ($O^{\delta-}$ species). Hence, the association reaction of $C^{\delta+}$–$O^{\delta-}$ and $O^{\delta-}$ species results in high catalytic activity for CO oxidation with low E_a.

2.1.2.4 Cross-coupling reactions. The cross-coupling reaction is one of the most practiced classes of catalytic C–C bond

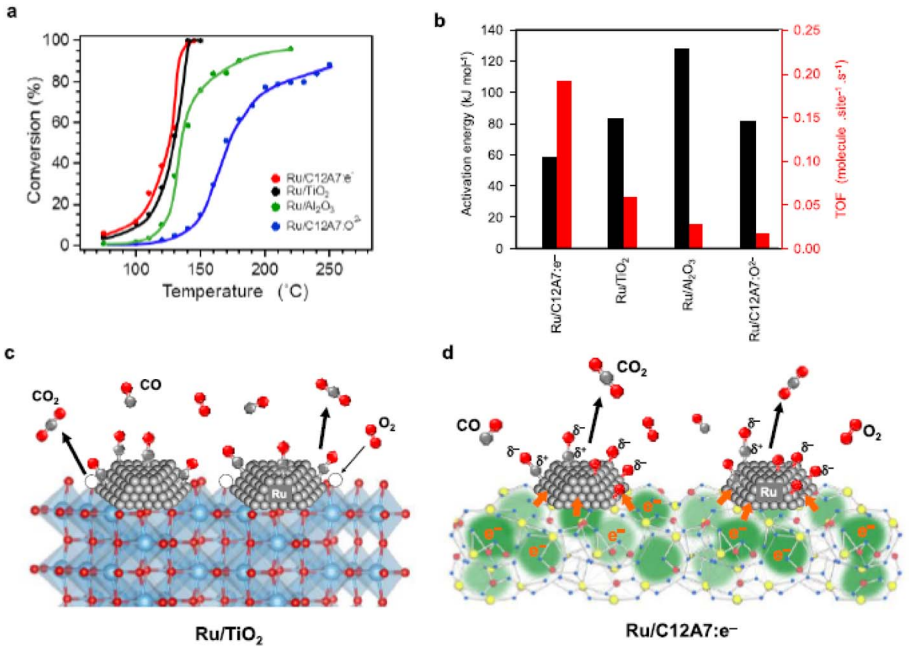

Fig. 11 (a) Catalytic activity for CO oxidation over various supported Ru catalysts. (b) TOFs and activation energies of the tested Ru catalysts. (c and d) Reaction pathways for CO oxidation on (c) Ru/TiO_2 and (d) $Ru/C12A7:e^-$. Copyright 2015, American Chemical Society.

formation. Because of the high activation barriers of the substrates associated with the rate-limiting elementary step, most cross-coupling reactions, especially those run over heterogeneous Pd catalysts, strongly rely on electron-rich Pd active sites.[63] $C12A7:e^-$ electride is an ideal support for achieving electron-rich Pd species because of its unique electronic properties associated with high carrier density and low work function (LWF). However, $C12A7:e^-$ cannot be applied to aqueous reactions owing to its water sensitivity. Moreover, the extremely low specific surface area of $C12A7:e^-$ restricts the dispersion of Pd metal.

Recently, our group designed a multistep electron transfer process through an intermediate graphene layer over an electride composite material, $Pd/Gr/C12A7:e^-$, in which nanometric Pd clusters were highly dispersed on graphene encapsulated $C12A7:e^-$ electride (Fig. 12a).[64] The graphene layer serves as an excellent electron transport medium, promoting electron transfer from the internal $C12A7:e^-$ electride through external Pd active sites to the aryl halide substrates. The multistep electron transfer process on the $Pd/Gr/C12A7:e^-$ catalyst was supported by performing Raman and XPS experiments, in which a blue shift of the G-band of the Gr layer (Fig. 12b) as well as a lower energy shift of the Pd 3d peak (Fig. 12c) emerged after the addition of $C12A7:e^-$. The electron transfer process is illustrated in Fig. 12d. $C12A7:e^-$ electride with a low work function ($\Phi_{WF} = 2.4$ eV) is considered an electron donor for Gr ($\Phi_{WF} = 5.0$ eV), leading to an electron transfer from $C12A7:e^-$ to Gr. Because of the comparable work functions of Gr ($\Phi_{WF} = 5.0$ eV) and Pd ($\Phi_{WF} = 5.1$ eV), the electron flows smoothly between Gr and Pd, allowing for negatively charged Pd species. Consequently, this composite material host has a strong electron donating ability associated with both highly dispersed and negatively charged Pd species, affording Suzuki cross-coupling reactions with over 20 times higher turnover frequencies and ~30% reduced activation energies compared to previously studied Pd-based catalysts (Fig. 12e). Impressively, the catalyst can also trigger various carbon–carbon cross-coupling reactions, such as Suzuki, Sonogashira, Stille, Hiyama and Heck coupling, with high activities.

It has also been reported that the Gr layer protects $C12A7:e^-$ electride against water. A Suzuki coupling reaction was performed over $Pd/Gr/C12A7:e^-$ powder with and without water-impregnation. The reaction rate remained almost unchanged, and the black color of the sample also remained (Fig. 12f). In the absence of a protective layer of Gr, the catalytic activity of the $Pd/C12A7:e^-$ catalyst was obviously degraded after water impregnation, and the sample color became light grey, which is associated with the transformation of the related Ca and Al hydrates. Mechanistic studies have demonstrated that the highly negatively charged Pd sites induce electron injection into the antibonding orbitals of C-X (X = I, Br), thus promoting the activation of aryl halides with various coupling partners under mild conditions.

2.1.2.5 Electrochemical reactions. Because of its metallic nature and small work function properties, $C12A7:e^-$ is also used as a novel cathode material in important electrochemical reactions. Li *et al.* reported the electrochemical transformation of the hydroxylation of *p*-(methylthio)-phenylboronic acid into *p*-(methylthio)phenol using $C12A7:e^-$ as an electrode.[65] Compared with traditional Pt and glassy carbon (GC) electrodes, the $C12A7:e^-$ electrode showed a significantly higher cathodic current for producing superoxide ions. Accordingly, the yield of *p*-(methylthio)phenol over the $C12A7:e^-$ electrode was as high as 90%, outperforming Pt (65%) and GC (79%) electrodes.

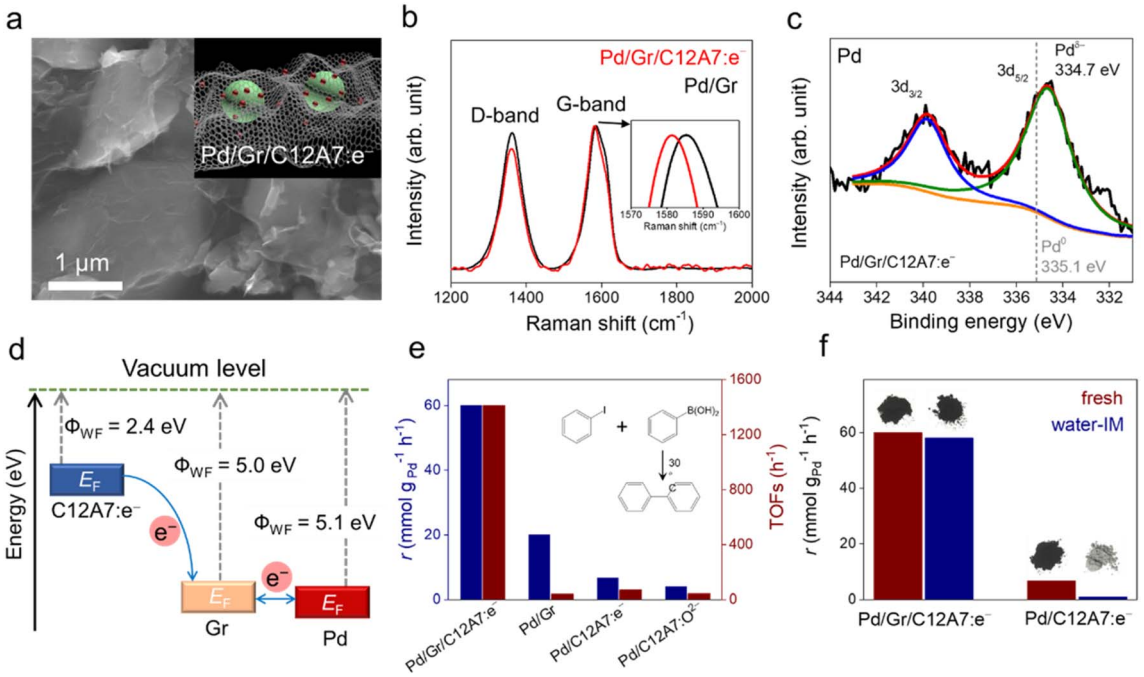

Fig. 12 (a) Representative SEM image of the Pd/Gr/C12A7:e$^-$ composite catalyst. Inset schematic illustration of the structure of Pd/Gr/C12A7:e$^-$. (b) Raman spectra of Pd/Gr/C12A7:e$^-$ and Pd/Gr. The G-mode shift is magnified in the inset. (c) XPS spectra of Pd 3d in Pd/Gr/C12A7:e$^-$. The grey dashed line represents the binding energy of the reference Pd metal with a zero valence state. (d) Comparison of the Fermi level in the C12A7:e$^-$ electride, Gr and Pd metal. Blue arrows indicate the direction of electron transfer from C12A7:e$^-$ to Gr and Pd metals. (e) Reaction rates and TOFs for the coupling of iodobenzene and phenylboronic acid over Pd/Gr/C12A7:e$^-$, Pd/Gr, Pd/C12A7:e$^-$ and Pd/C12A7:O^{2-} catalysts. (f) Reaction rates over fresh and water-impregnated (IM) Pd/Gr/C12A7:e$^-$ and Pd/C12A7:e$^-$ for the coupling of iodobenzene and phenylboronic acid with photographs of the corresponding catalyst powders. Copyright 2023, Royal Society of Chemistry.

In addition to the hydroxylation of arylboronic acid, Li *et al.* also found that C12A7:e$^-$ electrode shows good affinity to CO_2 and the inhibition of CO_2 reduction, which is favored for the monocarboxylation of various olefins.[66] In galvanostatic electrolysis under a CO_2 atmosphere, the monocarboxylic products were obtained with a higher yield (91%) than those at Pt (9%) and GC (32%) electrodes. Cyclic voltammetric analysis, together with galvanostatic electrolysis, demonstrated that the olefin was first reduced at the cathode to generate radical anion and then reacted with adsorbed CO_2 immediately to form the corresponding monocarboxylic products.

Regarding the applications of C12A7:e$^-$ in electrochemical transformations, researchers have recently turned their attention to the development of high-efficiency oxygen reduction reaction (ORR) electrocatalysts. Khan *et al.* developed Sn-doped C12A7:e$^-$ composite material and applied it to a highly active and durable electrocatalyst in the ORR.[67] Both the onset potential and current density of Sn-doped C12A7:e$^-$ are similar to commercial Pt/C catalysts. Not limited to electrocatalysis, the application of C12A7:e$^-$ in the field of photocatalysis is also studied by Hu *et al.*[68] They reported C12A7:e$^-$ as an electron promoter to P25 in a hydrogen evolution reaction (HER) from water through the photocatalysis process. The H_2 production rate reached 663 μmol h^{-1} g^{-1}, which was 43.9 times higher than that of pure P25. Mechanistic studies indicated that the introduction of C12A7:e$^-$ promoted the efficient separation of photogenerated electron–hole pairs of P25, resulting in the formation of a built-in electric field from P25 to C12A7:e$^-$ owing to the work function difference. The above electrocatalysis reactions are conducted in the aqueous phase. However, it is noteworthy that the crystal structure of C12A7:e$^-$ is not stable in water and slowly decomposes to form a Ca–Al–O–OH gel as an aluminous cement, leading to the release of anionic electrons. Therefore, we consider that the crystal and electronic structures of C12A7:e$^-$ after aqueous reactions should be identified carefully through detailed characterization.

Summarizing these encouraging advances, one may perceive that for C12A7:e$^-$-based catalysts, the electronic structure modification of the loaded active metal *via* strong electron donation power of C12A7:e$^-$ support creates a scenario to alter the bonding geometry and electronic nature of the reacting species, which is critical for the improvement of both activity and selectivity of heterogeneous metal-loaded catalysis.

2.1.3 Reductive reagent

2.1.3.1 Pinacol coupling reaction of aldehydes. In an aqueous medium, electrons are released from C12A7:e$^-$ electride by the decomposition of the Ca–Al–O framework in solution. Thus, C12A7:e$^-$ electride can be viewed as a solid form of solvated electrons. It can not only be used as an efficient support in catalysis, but the electrons of its framework can also operate as a reducing reagent in organic synthesis. In 2007, Buchammagari *et al.* first used C12A7:e$^-$ as a reductive reagent for the pinacol coupling of aromatic aldehydes.[69] When C12A7:e$^-$ and benzaldehyde are mixed in water, C12A7:e$^-$ electride gradually

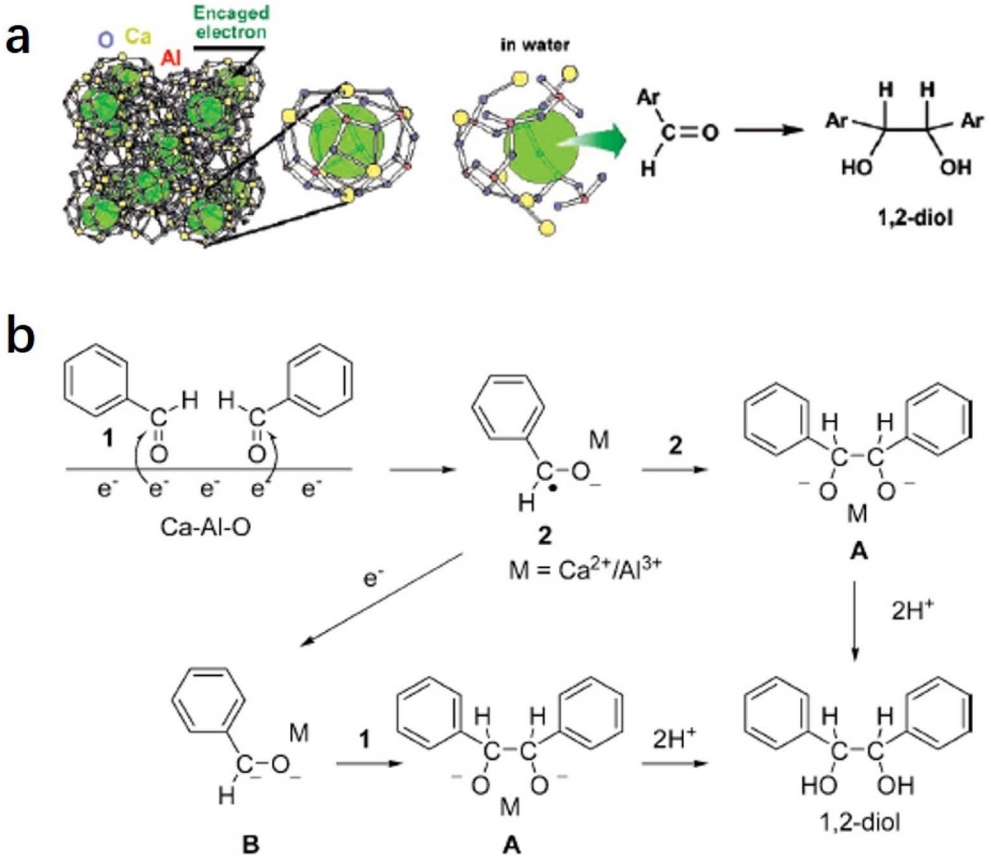

Fig. 13 (a) The C12A7:e$^-$ electride was employed for a pinacol coupling reaction in aqueous media. The Ca–Al–O gel formed by the destruction of the crystal structure of the C12A7:e$^-$ by water media played a key role in transferring the electron to electrophilic aldehydes. (b) Scheme of a possible mechanism for pinacol coupling mediated by C12A7:e$^-$. Copyright 2007, American Chemical Society.

dissolves, and the black powder transforms into a white gel. The white gel is hydrolyzed by hydrochloric acid aqueous solution and then extracted with Et_2O to produce 1,2-diphenylethyleneglycol (Fig. 13a).

After the reaction with water, a gel layer is formed on the surface of C12A7:e$^-$, which is similar to the hydrolysis of aluminous cement. A plausible mechanism for the pinacol coupling promoted by the C12A7:e$^-$ is shown in Fig. 13b. The carbonyl group of the aldehyde accepts the electrons released from the decomposed C12A7:e$^-$. The formed anion radicals are concentrated at the surface and coordinated to the surface Ca^{2+} or Al^{3+} cations (2). After that, two coordinated anion radicals undergo a dimerization reaction to form a pinacolate dianion (A). The dimerization of the anion radical coordinated with the metal forms the pinacolate dianion (A). Moreover, dianion (B) may also be formed by the one-electron reduction of (2). A nucleophilic addition of dianion (B) to the carbonyl group of aldehydes also yields A. Both pathways enable the formation of C–C bonds in the pinacol coupling reactions.

2.1.3.2 Reduction and oxidation of ketones. Inspired by the water-mediated pinacol coupling reaction over C12A7:e$^-$, Kim *et al.* reported the utilization of C12A7:e$^-$ electride as an electron source for the chemoselective oxidation and reduction of ketones in water (Fig. 14a).[70] The selectivity of the reaction can be controlled by the radical species of the transient intermediates. This controlled process is achieved by the reaction of the electrons of C12A7:e$^-$ with diketone or O_2, which leads to the formation of ketene dianions and superoxide radicals, respectively. Water plays two important roles in chemoselective reactions: one is the release of anionic electrons by reacting with C12A7:e$^-$, and the other is the electron solvation by water molecules mediated by transferring the anionic electrons to the substrates. The evolution of hydrogen gas demonstrated water splitting by electrons. Then, chemoselective reduction and oxidation are controlled by the electron transfer pathway.

As shown in Fig. 14b, in the reduction reaction, 1,2-diketone accepted two electrons from the solvated electron by water. After that, the two ketyl radical anions of 1,2-diketone quickly convert to enediol dianions *via* a radical dimerization process. The enediol dianion is protonated by a protic solvent, subsequently forming an enediol intermediate that undergoes tautomerization to generate α-hydroxy ketone. In the oxidation reaction, the electrons are first transferred to the oxygen molecule to facilitate the formation of superoxide radicals. These superoxide radical anions then react with benzil, resulting in the formation of α-peroxy ketone intermediate. It is also proposed that the utilization of electrides may be an alternative to the pulse radiolysis of water in synthetic chemistry.

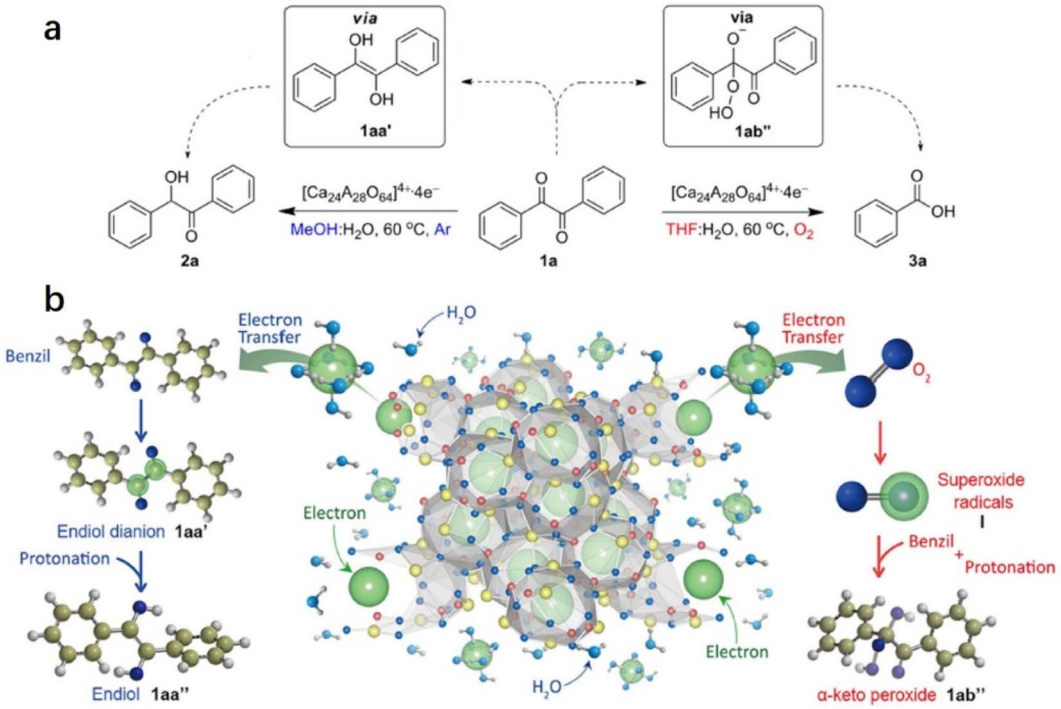

Fig. 14 Strategies for the chemoselective reduction and oxidation of 1,2-diketones using the C12A7:e$^-$ electride. (a) The chemoselective reduction and oxidation of benzil using the C12A7:e$^-$ electride. (b) Schematic illustration of the chemoselective reduction and oxidation of benzil by controlling the electron transfer pathway to benzil or O_2 *via* the release of electrons from the C12A7:e$^-$ electride *via* hydrolysis as well as the possible solvation of electrons by water molecules. Copyright 2015, Springer Nature.

2.1.3.3 CO_2 reduction. Because CO_2 is an important greenhouse gas, the conversion of CO_2 into useful chemicals, such as CO, provides a highly promising way for sustainable development. Because of the nonpolar and linear double bonds of CO_2 molecules, the activation of CO_2 normally requires either harsh conditions or active reducing agents. Toda *et al.* reported that CO_2 can be split by C12A7:e$^-$ at room temperature, in which a high concentration of localized electrons in the near-surface region and a corrugation of the C12A7 surface can trap O atoms as well as strain CO and CO_2 molecules.[71]

On C12A7:e$^-$ surface, the cage structures are occupied by anionic electrons, which also serve as anchor sites for trapping CO_2 and CO. Because the surface of C12A7 is corrugated, there are five possible configurations of the molecule adsorption: (1) physisorbed CO_2, (2) bent $CO_2^{\delta-}$, (3) tridentate CO_2 and (4, 5) dissociated CO + O (Fig. 15a). In the TPD measurement

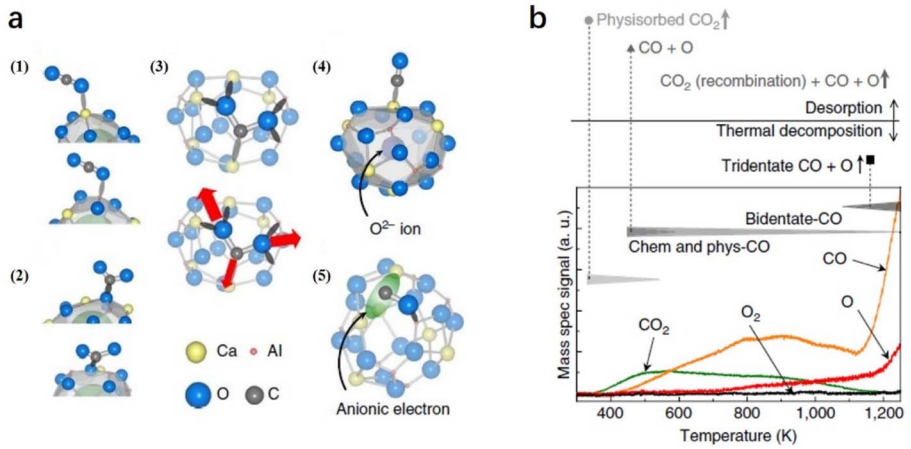

Fig. 15 (a) Geometrical configurations of a CO_2 molecule adsorbed on C12A7:e$^-$ surface. (b) TPD curves of all desorption products from the C12A7:e$^-$ surface after 2 L of exposure to CO_2 at RT with the proposed CO_2 desorption and decomposition sequence. The intensities of the curves were calibrated using sensitivity factors. Copyright 2013, Springer Nature.

(Fig. 15b), physisorbed CO_2 and CO started to desorb at 350 and 400 K, respectively. At temperatures above 400 K, a small amount of CO_2 desorption stemmed from partial CO and O recombination. Moreover, this recombination is restrained above 700 K owing to O atom desorption. At temperatures above 1100 K, the total physisorbed CO_2 and most of the CO leave the surface. Additionally, the deep trapped CO_2 (tridentate configuration) is decomposed, causing a rapid increase in CO and O desorption. Because reductive species, such as metallic alkali or alkaline earth metals or harsh reaction conditions, are not required, C12A7:e^- is considered a promising reducing agent for CO_2 activation and splitting.

2.2. O^- and O_2^- substitution

Oxygen usually exists as a divalent anion O^{2-} in oxide crystals. There are a few cases where oxygen forms active species, such as O^-, O_2^-, and O_2^{2-}, because these active oxygen species are highly unstable and difficult to obtain in large quantities, especially for O^- with extremely strong oxidation power.[70,72] If a material can store a large amount of active oxygen species in a chemically and thermally stable form, it is expected to exhibit unique chemical properties. C12A7 has a positively charged framework $[Ca_{24}Al_{28}O_{64}]^{4+}$ that possesses 12 interconnected nanocages with a diameter of *ca.* 0.4 nm, providing opportunities to store various anions. Normally, O^{2-} counter anions occupy the cages of C12A7 (C12A7:O^{2-}).[9] These encaged O^{2-} can be substituted by active oxygen species (O^- and O_2^-), resulting in stable storage of these active oxygen species in the cage of the C12A7. Thus, it is anticipated that the obtained C12A7:O^- and C12A7:O_2^- exhibit great performance in some important chemical reactions.

2.2.1 Preparation method. Generally, the active oxygen species are created on the surface of solid oxides using energetic photons, such as X-ray irradiation.[73] However, in C12A7, the active oxygen species can be obtained simply through a solid-state reaction of stoichiometric $CaCO_3$ and γ-Al_2O_3 in an oxidative atmosphere.[11,12,34,74–78] In 1987, Hosono *et al.* reported the presence of the active oxygen species (O_2^-) in C12A7 crystal.[74] After that, Hayashi *et al.* found that high oxygen partial pressure favors the formation of active oxygen species, especially O^- [12]. The dry oxygen ($pO_2 = 1$ atm, $pH_2O = 6 \times 10^{-5}$ atm) treated C12A7 contains a large amount of O^- and O_2^- with anionic concentrations of 2×10^{20} cm^{-3} and 4×10^{20} cm^{-3}, respectively. Then, they treated C12A7 in pressurized oxygen up to 400 atm and found that the concentrations of the incorporated O_2^- and O^- can be elevated to 1.7×10^{21} cm^{-3}, which corresponds to *ca.* three-fourths of the theoretical maximum.[11] The concentrations of O^- and O_2^- are comparable in C12A7, and the formation mechanism can be explained using the following equations: molecular O_2 diffuses into the lattice and accepts an electron from the free O^{2-} ion:

$$O_2\ (\text{atmosphere}) \rightarrow O_2\ (\text{cage})$$

$$O^{2-}\ (\text{cage}) + O_2\ (\text{cage}) \rightarrow O^-\ (\text{cage}) + O_2^-\ (\text{cage})$$

Matsuishi *et al.* observed the hyperfine splitting of O_2^- in a C12A7 single crystal with the treatment of $^{17}O_2$ at 550 °C, providing solid evidence that encaged O_2^- derived from gaseous O_2 in the atmosphere.[77]

Yang *et al.* studied the formation mechanism of active oxygen species in C12A7, including O^-, O_2^-, and O_2^{2-}.[75] For O_2^{2-}, it may be formed *via* the reaction of O_2 with the engaged free oxygen:

$$2O^{2-}\ (\text{cage}) + O_2\ (\text{cage}) \rightarrow 2O_2^{2-}\ (\text{cage})$$

or *via* the combination of two O^-:

$$2O^-\ (\text{cage}) \rightarrow O_2^{2-}\ (\text{cage})$$

These oxygen species in C12A7 become mobile and can be desorbed at above 600 °C. When heating C12A7 in O_2 at temperatures higher than 400 °C, these oxygen species can also be regenerated. The desorption of oxygen species occurs in a manner that reverses the formation processes (Fig. 16).

2.2.2 Oxidative reaction

2.2.2.1 Super oxidative property. Hayashi *et al.* reported that the O^--encaged C12A7 exhibits superior oxidative reactivity, which can even oxidize the precious metal Pt.[12] As shown in Fig. 17a, O^--encaged C12A7 was attached to a plate of Pt metal, and the plate was annealed at 1350 °C in wet and dry oxygen (Fig. 17a). The O^--encaged C12A7 contacted area became brown in dry oxygen, while the wet oxygen treated one remained colorless. The subsequent XPS characterization verified the presence of the tetravalent state of Pt(VI) (Fig. 17b), indicating that Pt metal could be oxidized by oxygen radicals embedded in C12A7 during dry oxygen treatment.

2.2.2.2 Partial oxidation of methane. Owing to the increasing awareness of human environmental protection, clean energy, such as hydrogen, is urgently needed. The partial oxidation of methane is regarded as a potential route to obtaining hydrogen.[79–81] Compared with methane reformed by steam and CO_2, methane oxidation reaction is thermodynamically much favored. Moreover, the ratio of the product, which is 2 : 1 for H_2 and CO, exactly matches the feed ratio for Fischer–Tropsch syntheses (Fig. 18a).[82] The high oxidative properties and controlled oxygen radicals offer C12A7 a special ability for the oxidation of methane.

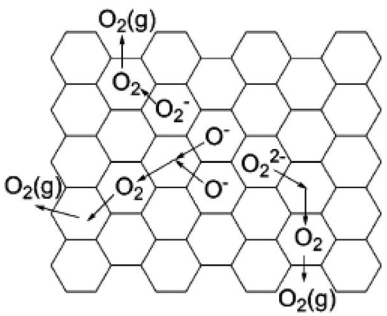

Fig. 16 The model for the desorption of oxygen radicals (O^-, O_2^-, and O_2^{2-}) in C12A7. Copyright 2004, American Chemical Society.

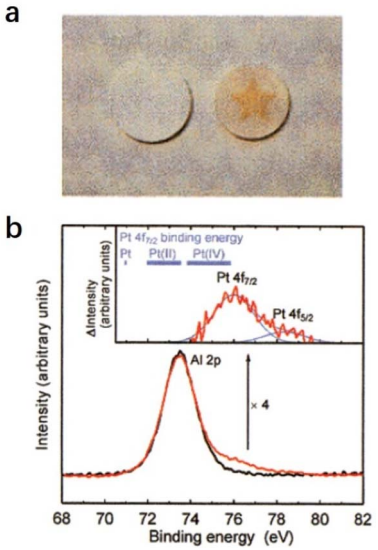

Fig. 17 (a) Photographs of the C12A7 ceramics sintered in wet air (left) and dry oxygen (right). (b) XPS spectra for the brown-colored area (red line) and the uncolored area (black line). Inset is the difference between the two spectra. Copyright 2002, American Chemical Society.

In 2004, Yang *et al.* reported various transition metals, such as Ni, Co, Pt, Pd and Ru, supported C12A7 are efficient in the partial oxidation of methane.[83] Through the investigation of the metal type, reaction temperature and space velocity, Pt/C12A7 and Ni/C12A7 are the optimal catalysts for the reaction, which offered a relatively high selectivity and stability even under mild conditions (Fig. 18b–d). They attributed the counterintuitive high activity of the C12A7 catalyst to two factors: (1) the unique surface cages of C12A7 allow for high dispersion of metal; (2) the active oxygen species of C12A7 ensure a high coke resistance ability.

2.2.2.3 Steam reforming of bio-oil. Hydrogen is regarded as an ideal green energy carrier, and the main route of hydrogen products is the catalytic steam reforming of fossil fuels, such as natural gas, oil-derived naphtha, partial oxidation of heavy oils, and coal gasification.[84–86] The production of a large amount of carbon dioxide causes serious environmental issues. The development of clean alternatives to produce hydrogen has attracted considerable attention. As an environmental and renewable source, biomass is widely accepted as a promising raw material for hydrogen production.[87,88] The most efficient route for the generation of hydrogen from biomass should be catalytic steam reforming of bio-oil with the combination of a water gas shift reaction (Fig. 19a).[89]

Wang *et al.* reported a group of early transition metals supported C12A7:O^- catalysts (C12A7:O^-/M, M = Mg, K, and Ce), which can be employed to promote hydrogen production from bio-oil.[90] Based on the detailed investigation of the loaded metal types and reaction conditions, it is found that the hydrogen yield over the C12A7:O^-/18% Mg catalyst was as high as 80% with a carbon conversion of nearly 100% (Fig. 19b and c). They attributed the high catalytic performance of C12A7:O^-/18% Mg to the incorporated O^- species, in which O^- promotes the formation of OH^- and effectively suppresses carbon deposition.

2.2.2.4 Formation of phenol. As one of the most important chemical raw materials, the annual global demand for phenol is approximately 10 million tons. Generally, a multi-stage cumene process is required to synthesize phenol in industry, resulting in a certain amount of co-production of acetone and by-products, such as *n*-propylbenzene and diisopropylbenzene.[91] It is well known that the active oxygen from the decomposition of nitrous oxide plays a key role in phenol formation.[92] Conventionally, the generation of active oxygen needs to undergo a complex and costly process using energetic irradiations.[73]

Inspired by the unique behavior of O^- storage and emission in C12A7, Dong *et al.* reported a direct synthesis of phenol through the hydroxylation of benzene by O^- and OH^- anions of C12A7.[93] As shown in Fig. 20a, O^- species incorporated in C12A7 were regarded as the active species for the initial conversion of benzene ($C_6H_6 + O^- \rightarrow C_6H_5 + OH^-$). After that, the as-produced C_6H_5 reacts with OH^- to form $C_6H_5OH^-$ intermediate species. Finally, phenol can be released by a detachment process ($C_6H_5OH^- \rightarrow C_6H_5OH + e^-$). The atomic efficiency of such processes is quite high, and the selectivity of phenol reaches nearly 100% (Fig. 20b and c).

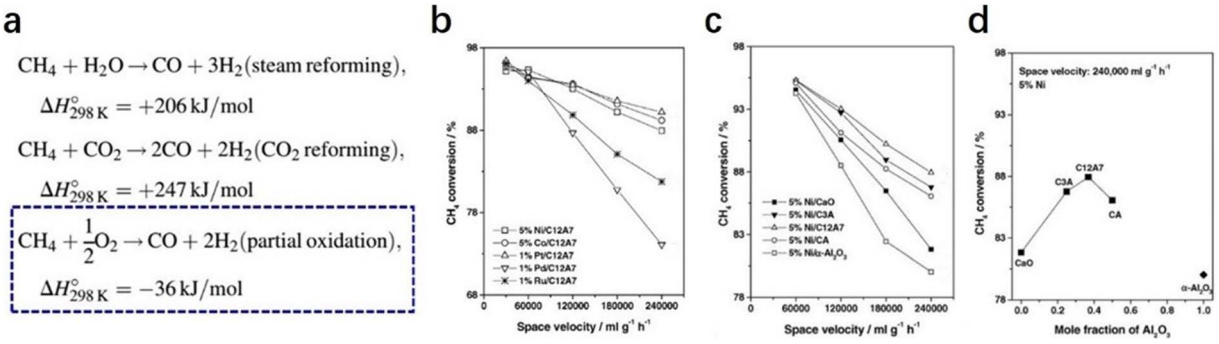

Fig. 18 (a) Three routes of CH_4 oxidation. (b) Conversion of CH_4 partial oxidation to syngas over promoted C12A7 at 800 °C as a function of space velocity: 5% Ni/C12A7; 5% Co/C12A7; 1% Pt/C12A7; 1% Pd/C12A7; and 1% Ru/C12A7. (c and d) CH_4 partial oxidation to syngas over Ni catalysts supported on different supports at 800 °C as a function of space velocity (c) and as a function of a mole fraction of Al_2O_3 in the supports (d): 5% Ni/CaO; 5% Ni/C3A; 5% Ni/CA; 5% Ni/C12A7; and 5% Ni/α-Al_2O_3. Copyright 2004, Elsevier.

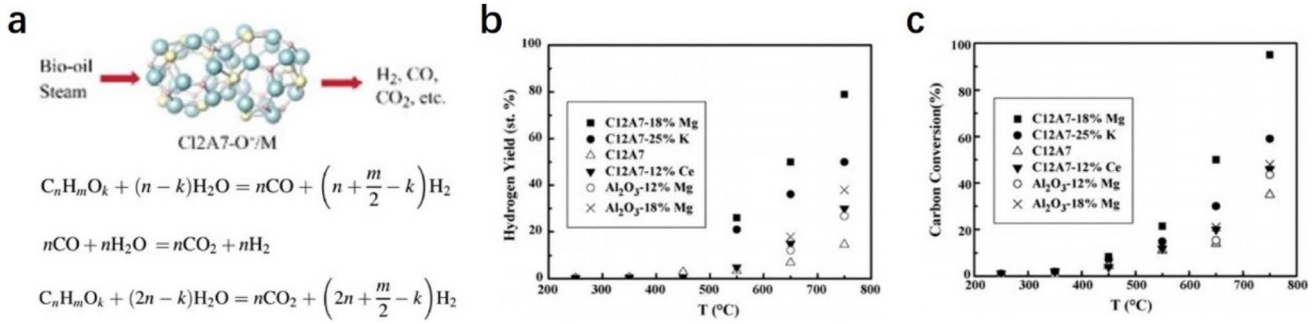

Fig. 19 (a) Steam reforming of biomass. The hydrogen yield (b) and (c) carbon conversion from the catalytic steam reforming of the bio-oil were measured as a function of temperature over various catalysts. Copyright 2007, Elsevier.

2.2.3 Reduction reaction

2.2.3.1 Selective N_2O removal. N_2O, an undesired byproduct but unavoidable emission in the industry reaching about 4 million tons per year, causes serious environmental issues, such as photochemical oxidation, acid rain, and climate deterioration.[94] To reduce the emission of N_2O, catalytic decomposition is one of the most cost-effective solutions. An anionic redox mechanism initiated by oxygen atom transfer was proposed for N_2O decomposition.[95] It comprises two principal reaction steps: N–O bond breaking with the oxygen atom transfer to the surface and the formation of the peroxy intermediate ($N_2O + O_{surf}^{2-} \rightarrow N_2 + O_{2surf}^{2-}$). The O–O bond can be formed by the recombination of oxygen atoms *via* the surface diffusion of peroxy species ($2O_{2surf}^{2-} \rightarrow 2O_{surf}^{2-} + O_2$). Because of the key role of the oxygen anions, C12A7 with the excellent storage capacity of active oxygen anions is expected to show great potential in N_2O decomposition.

Ruszak *et al.* employed C12A7 as a catalyst for the N_2O decomposition process.[96] The trapped active oxygen species in C12A7 were identified by electron paramagnetic resonance (EPR) and Raman spectra (Fig. 21a). It is proposed that the transfer of oxygen species from the cage sites to the surface at high temperatures plays a key role in the decomposition of N_2O. The abundant surface active oxygen promoted the abstract of oxygen from N_2O. The conversion of the decomposed nitrous oxide reached *ca.* 90% upon 1150 K (Fig. 21b and c).

2.2.3.2 NO_x reduction. The selective catalytic reductions (SCRs) of NO_x by ammonia ($4NO + 4NH_3 + O_2 \rightarrow 4N_2 + 6H_2O$) or hydrocarbons (NO + hydrocarbons $\rightarrow N_2 + CO_2 + H_2O$) are well-known approaches for reducing the emission of vehicle exhaust.[97] However, the SCR route requires accurate control of the stoichiometric of ammonia and hydrocarbons. For the NO_x storage/reduction (NSR) route, NO_x can be stored in the catalyst during the oxygen lean period. Moreover, under oxygen-rich conditions, the encaged NO_x is decomposed and subsequently reduced to nitrogen.[98] To date, Ba-based catalysts are the most effective for NSR. However, it is easy to react with the sulfur impurity in real exhaust gases, which forms stable sulfates and inhibits the reaction, leading to the deactivation of the catalysts.[99] Based on the storage and emission capacities of the active O^- species of C12A7, Gao *et al.* developed a new NSR catalyst of K-doped C12A7:O^-, in which the engaged O^- can react with adsorbed NO and transform to NO_3^- and/or NO_2^-, avoiding the formation of stable sulfates.[100] The NO_x conversion of K-doped C12A7:O^- can reach nearly 80% with the selectivity of N_2 approaching 100%.

2.3. H^- substitution

Hydrogen can operate as both an electron donor and acceptor owing to its medium electronegativity, and the charge states of hydrogen can be divided into H^+ (proton), H^0 (atomic hydrogen), and H^- (hydride ion). The properties of hydrogen with different charge states quite differ from each other. Compared with H^+ and H^0, H^- ions have rarely been investigated because of the instability of hydride ions. Interestingly, the positively charged sub-nano-cages of C12A7 provide a unique structure for stabilizing H^- ions and forming C12A7:H^-.

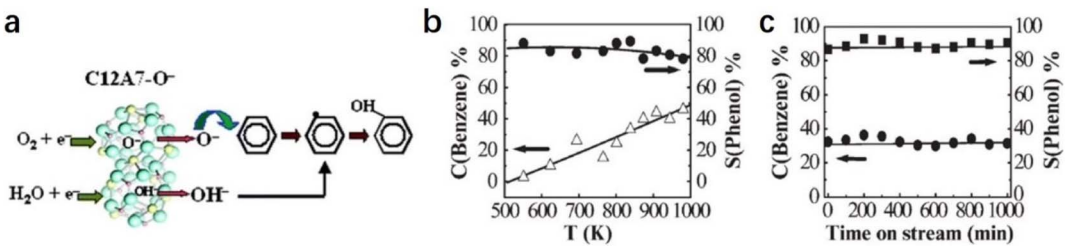

Fig. 20 (a) Synthesis of phenol using the O^- and OH^- anions in C12A7 to directly hydroxylate the aromatic ring of benzene. (b) Effect of reaction temperature, and (c) stability of the catalyst with reactant mixture. Copyright 2005, Royal Society of Chemistry.

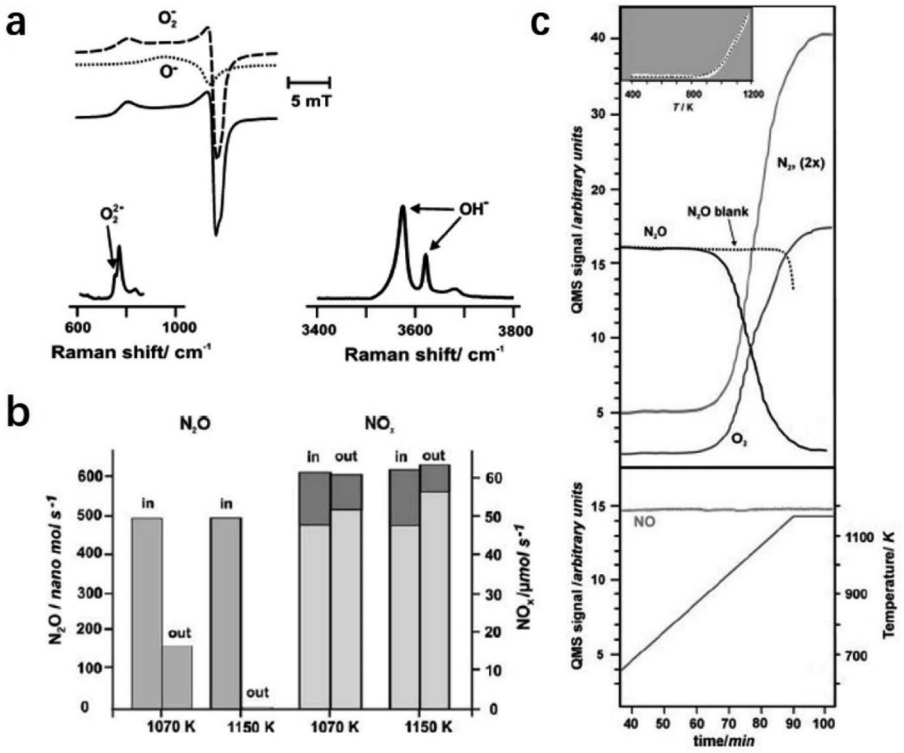

Fig. 21 (a) Spectroscopic characterization of extra-framework anions present in mayenite. EPR spectrum of O_x^- species (solid line) and the simulated component signals of O^- and O_2^- radicals (dashed lines) (top). Raman spectra of O_2^{2-} (left down) and OH^- cage species (right down). (b) Catalytic screening of N_2O decomposition performed in a pilot plant at 1070 and 1150 K using a real process gas feed. The bars represent the N_2O and NO (light grey) and NO_2 (dark grey) compositions in the inlet and outlet of the reactor. (c) TPSR profiles for N_2O decomposition tests performed on a laboratory scale over mayenite along with the associated N_2 and O_2 lines (top). The dotted line represents the blank experiment, whereas in the insert, the kinetic fit (black dotted line) to the experimental data (white dots) is shown. The NO line with the temperature profile was used in all the TPSR experiments (down). Copyright 2008, Springer Nature.

2.3.1 Preparation method. The H^--encaged C12A7 can be synthesized by either indirect or direct methods. The indirect synthesis of H^--encaged C12A7 can be performed by the reduction of C12A7 using pure H_2 gas[35] or metal hydrides (TiH_2 (ref. 101) or CaH_2 (ref. 13)) as reducing agents. H^- ions are incorporated into the nanocage structure of C12A7 through two steps: the substitution of O^{2-} ions of the surface cage of C12A7 by the H^- ions and, subsequently, the replacement of inside O^{2-} ions by the surface-incorporated H^- ions. The H^- ion concentration can reach the theoretical maximum of 2.3×10^{21} cm^{-3} when C12A7 was annealed with CaH_2 at 800 °C for 120 h.[13]

The direct synthesis of C12A7:H^- is achieved by a solid–state reaction under high pressure.[102] The reducing atmosphere is important for preventing the unintended incorporation of impurity ions, such as O^{2-} and OH^- ions. The high-pressure apparatus can provide a sealed environment for the reaction of the starting materials under reductive conditions. The C12A7:H^- with a high H^- concentration of $\sim 0.6 \times 10^{21}$ cm^{-3} was obtained by the reaction of CaO, Al_2O_3, and CaH_2 with molar ratios of 11 : 7 : 1. The reaction condition required a high pressure ranging from 0.5 to 0.75 GPa as well as a high temperature ranging from 1200 to 1300 °C. Excess CaH_2 is required as the H source for the incorporated H^- ions during the treatment of high pressure.

2.3.2 Photoelectron donor. H^- ions occupying halide ion sites in alkali-halide crystals have been known as the U center since the 1930s.[103] UV illumination ($\lambda \sim 300$ nm) enables the transformation of H^- to H^0 and electron.[104] However, the generated electron is localized at a halogen vacancy (F^+ center) and does not result in electrical conductivity. A similar photochemical conversion process is also detected on the surface of MgO.[105] In 2002, Hayashi and co-authors demonstrate that H^- ions in the cage of C12A7 can be photochemically converted to protons by releasing carrier electrons on UV illumination, allowing for persistent conductivity ($\sim$0.3 S cm^{-1}) (Fig. 22a).[38] The persistence of photoinduced conductivity is explained by the slow kinetics of the reverse process at room temperature.

A possible mechanism for the photo-induced conversion of C12A7:H^- from an insulator to a conductor is proposed: UV irradiation induces an electron emission from the encaged H^- ions ($H^- \rightarrow H^0 + e^-$). After that, Matsuishi *et al.* succeeded in observing the EPR signal of H^0 in C12A7 after UV illumination at 4 K (Fig. 22b).[35] The concentration of generated H^0 is almost equal to that of F^+ (Fig. 22c), which demonstrates that H^- is trapped in the cage of C12A7 and follows photo-dissociation to H^0 and F^+. Fig. 22d shows that the fractions of H^0 and F^+ remain

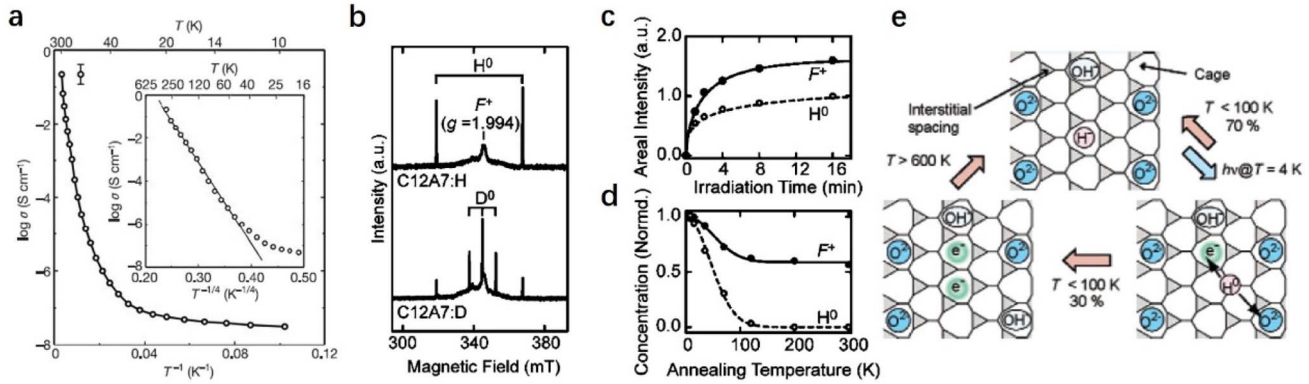

Fig. 22 (a) Electronic conduction after UV-irradiated C12A7:H^-. Copyright 2002, Springer Nature. (b) EPR spectra of C12A7:H and C12A7:D observed at 4 K after UV illumination. (c) Areal signal intensities of H^0 and F^+ as a function of UV illumination time. Almost 1 : 1 generation indicates photodissociation of H^-: $H^- \rightarrow H^0 + e^-$. (d) Isochronal annealing of H^0 and F^+. (e) Scheme of photoinduced insulator–conductor conversion. Copyright 2005, American Chemical Society.

unchanged after thermal treatment. Almost no H^0 was left after the treatment above ~200 K, while ~60% of the F^+ remains even at 300 K, implying that partial H^0 recombines with F^+ to form H^- ($H^0 + e^- \rightarrow H^-$), and the others have been removed differently without the consumption of the F^+. A plausible reaction of H^0 with free oxygen to form OH^-, yielding additional F^+: $H^0 + O^{2-} \rightarrow OH^- + e^-$ (or $H^0 + H^0 \rightarrow H_2$), also contributes to the retention of F^+.

A similar mechanism was also proposed for MgO surfaces.[106] Nearly 70% of H^0 recombines with electrons, and the remaining H^0 reacts with free oxygen to form OH^-. The fraction of remaining F^+ is experimentally estimated to be ~60%. OH^- is quite stable in the cage of C12A7 and does not react with trapped electrons at room temperature. When C12A7:H^- is illuminated by UV light, several tens of percent of photoinduced electrons survive and yield hopping conductivity. At temperatures above ~600 K, the OH^- is reduced by trapped electrons to form H^- and O^{2-}, and therefore the conductivity is eliminated. The reactions proceed under UV illumination, as illustrated in Fig. 22e.

2.3.3 Anti-hydrogen poisoning of ammonia synthesis. As described in Section 2.1.2, C12A7:e^- significantly promotes the dissociation of N_2 through electron back donation from Ru, and the hydrogen poisoning of Ru surfaces can be suppressed owing to the reversible hydrogen storage ability of C12A7:e^-. Kitano *et al.* proposed a mechanism of ammonia synthesis involving reversible storage and the release of hydrogen on the surface of Ru/C12A7:e^- (Fig. 23).[49]

Recently, Kammert and co-workers reported that hydrogen is likely to be adsorbed on the catalyst surface rather than the

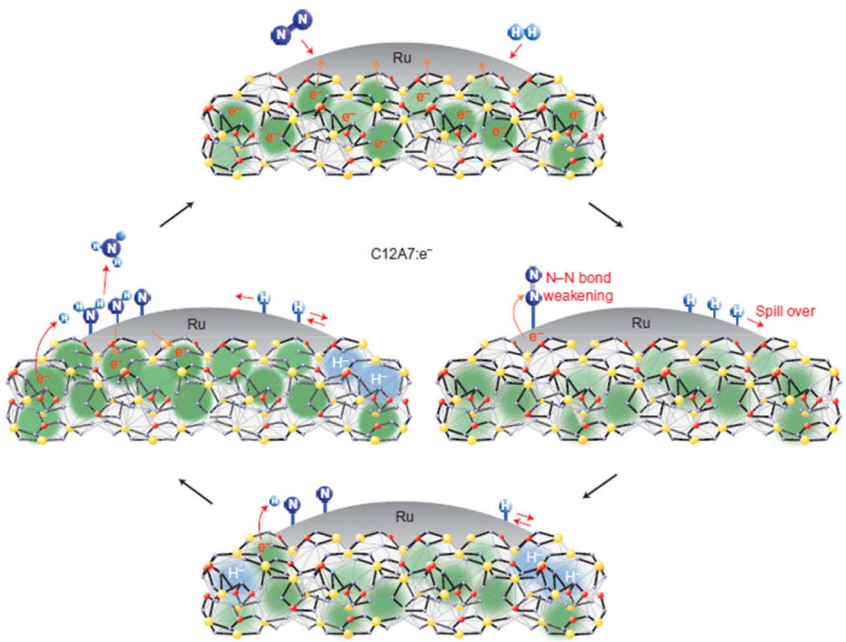

Fig. 23 Possible pathway for the ammonia synthesis reaction over Ru/C12A7:e^-. Copyright 2012, Springer Nature.

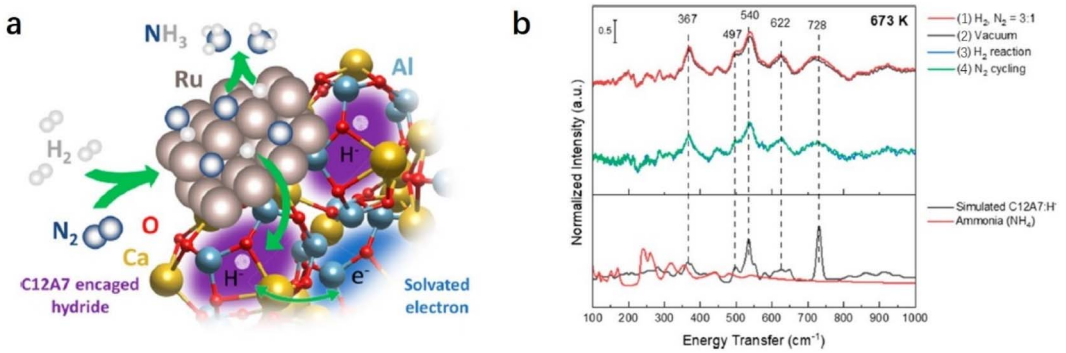

Fig. 24 (a) Schematic diagram of the ammonia synthesis reaction over Ru/C12A7:e$^-$. (b) The inelastic neutron-scattering spectra of Ru/C12A7:e$^-$ collected at 5 K after exposure to (1) 0.1 MPa 3 : 1 H_2 : N_2 mixture, (2) vacuum, (3) 0.1 MPa H_2, and (4) 5 cycles of 0.1 MPa N_2 at 673 K. Copyright 2020, American Chemical Society.

storage of H^- ion in the cage of C12A7:e$^-$, which plays a dominant role in NH_3 synthesis over Ru/C12A7:e$^-$ catalyst (Fig. 24a).[107] They provided evidence for the presence of H^- ions in the framework of Ru/C12A7:e$^-$ during NH_3 synthesis by *in situ* inelastic neutron-scattering spectroscopy (Fig. 24b). It is founded that the encaged H^- species are stable in the cage of C12A7:e$^-$, which are not involved in the formation of NH_3. Instead, dissociated hydrogen species on the Ru surface predominantly participate in ammonia synthesis. The extremely high coverage of nitrogen species on the surface of Ru/C12A7:e$^-$ is responsible for the anti-hydrogen poisoning over Ru. The RDS also shifted from N_2 cleavage to the formation of the N–H bond, which agrees with Kitano's study.

2.3.4 Selective hydrogenation of the heteroarene reaction. Selective hydrogenation of heteroarenes is of fundamental interest in organic synthesis and is applied on a large scale for the production of various fine and bulk chemicals.[108] It has been reported that the heterolytic cleavage of H_2 with the formation of $H^{\sigma+}$ and $H^{\sigma-}$ is beneficial for the selective hydrogenation of polar functional groups, such as heteroarenes.[109] In our study, hydrothermal-prepared C12A7 (HT-C12A7)-supported Ru catalysts are efficient for the chemoselective hydrogenation of different N-heteroarenes in a solvent-free system (Fig. 25a).[110] Compared with traditional metal oxide supports, C12A7-supported Ru offered a much higher yield of 1,2,3,4-tetrahydroquinoline under the same reaction conditions (Fig. 25b),

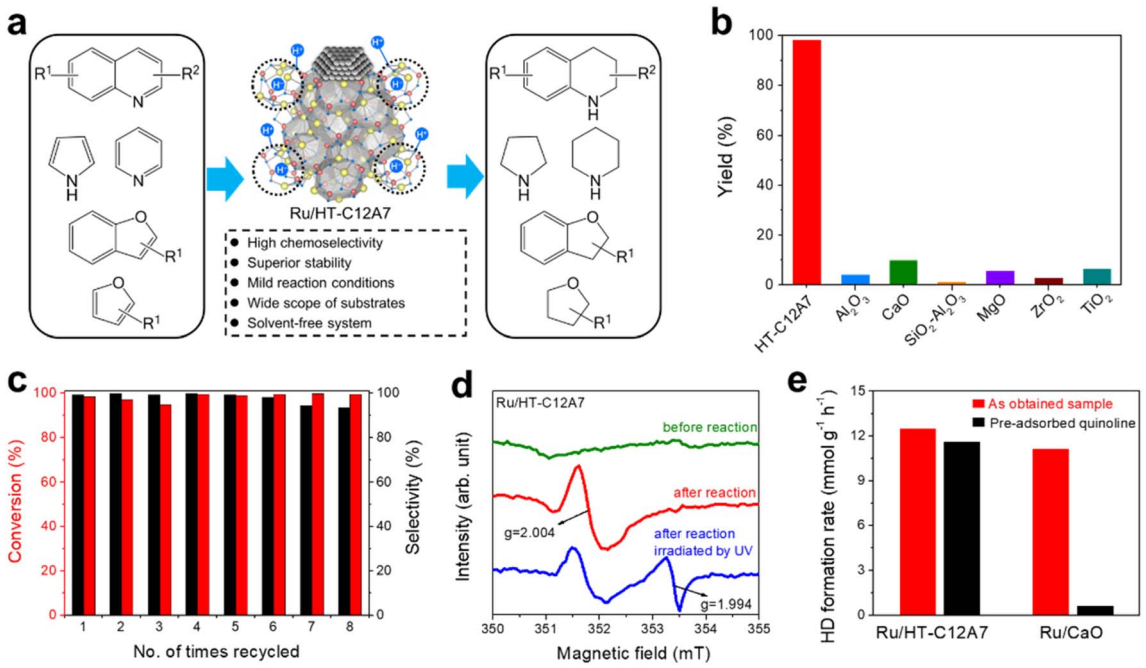

Fig. 25 (a) Multiple selective hydrogenation reactions on Ru/HT-C12A7. (b) Catalytic activities for the hydrogenation of quinoline over various Ru-based catalysts with different supports. (c) Recycle experiment for hydrogenation of quinoline over Ru/HT-C12A7. (d) EPR spectra for Ru/HT-C12A7 catalyst before and after hydrogenation reaction, and Ru/HT-C12A7 after reaction under UV light irradiation. (e) Rate of HD formation at 50 °C over Ru/HT-C12A7 and Ru/CaO with and without pre-adsorbed quinoline. Copyright 2017, Royal Society of Chemistry.

and the catalytic activity was well retained in eight consecutive runs (Fig. 25c). The superior catalytic performance can be attributed to the trapped H^- anions in the surface-truncated cages of C12A7, promoting the heterolytic dissociation of H_2 to yield $H^{\sigma+}$ and $H^{\sigma-}$ ion pairs. However, the abundant surface basic sites of C12A7 also function as anchor sites for stabilizing H^-, which can be verified by CO_2-TPD and EPR spectra results (Fig. 25d). H_2-D_2 exchange test indicates that the H_2 dissociation process on Ru/CaO is strongly inhibited through poisoning by quinoline adsorption. Additionally, there is no obvious change in the exchange rate over the Ru/HT-C12A7 catalyst, which demonstrates that quinoline molecules also play an important role in the heterolytic cleavage of H_2 over Ru/HT-C12A7 (Fig. 25e).

2.4. Metal single atom fixation

In recent years, single metal atom catalysts have been observed as rising stars for the green synthesis of fine chemicals owing to the ideal atomic utilization (100%).[111–114] Moreover, the electronic structure of isolated metal atoms can be easily modified using support materials. Unfortunately, a highly dispersed single atom catalyst is difficult to prepare because of the metal atoms with extremely high surface energy, which are easy to aggregate and sinter.[115] Defects are reported to be effective in stabilizing metal atoms; thus, different supports with rich surface defects are designed to prepare single atom catalysts.[116] Considering the unique electronic and geometric structure of C12A7, the positively charged nanocages provide the possibility of anchoring single metal atoms.

2.4.1 Pt single atom catalysis. As the "holy grail" of catalysts, Pt-based catalysts exhibit encouraging activity in various reactions. Unfortunately, the high cost and low abundance of Pt metal have always hindered its large-scale applications. Single-atom catalysis sheds new light on the efficient utilization of Pt metal catalysts. Recently, we reported that C12A7 can be used to stabilize a single Pt atom owing to the ideal size and electronic feature of the nanocavity structures (Fig. 26a).[36] The unique confinement effect of the nanocavity of C12A7 ensures remarkable thermal stability of Pt atoms even at reduction temperatures of up to 600 °C. Aberration-corrected high-angle annular dark-field scanning transmission electron microscopy (HADDF-STEM) proved the single atomic form of the trapped Pt species (Fig. 26b). From the results of the extended X-ray absorption fine structure spectra (EXAFS), it is also observed that Pt–Pt bonds are absent, further verifying that the Pt species are atomically dispersed in C12A7 (Fig. 26c).

In the hydrogenation reaction of 4-chloronitrobenzene, the turnover frequencies (TOFs) of Pt/C12A7 reach as high as 25 772 h^{-1}, which is one order of magnitude higher than those of Pt/CaO (3396 h^{-1}) and Pt/Al_2O_3 (1178 h^{-1}) under the same reaction conditions (Fig. 26d). The reaction mechanism of Pt/C12A7 can be revealed by the combination of kinetic isotope effect (KIE) and Fourier transform infrared (FTIR) spectroscopy. The large primary isotope ratio (k_H/k_D) of 4.7 indicates that the rate

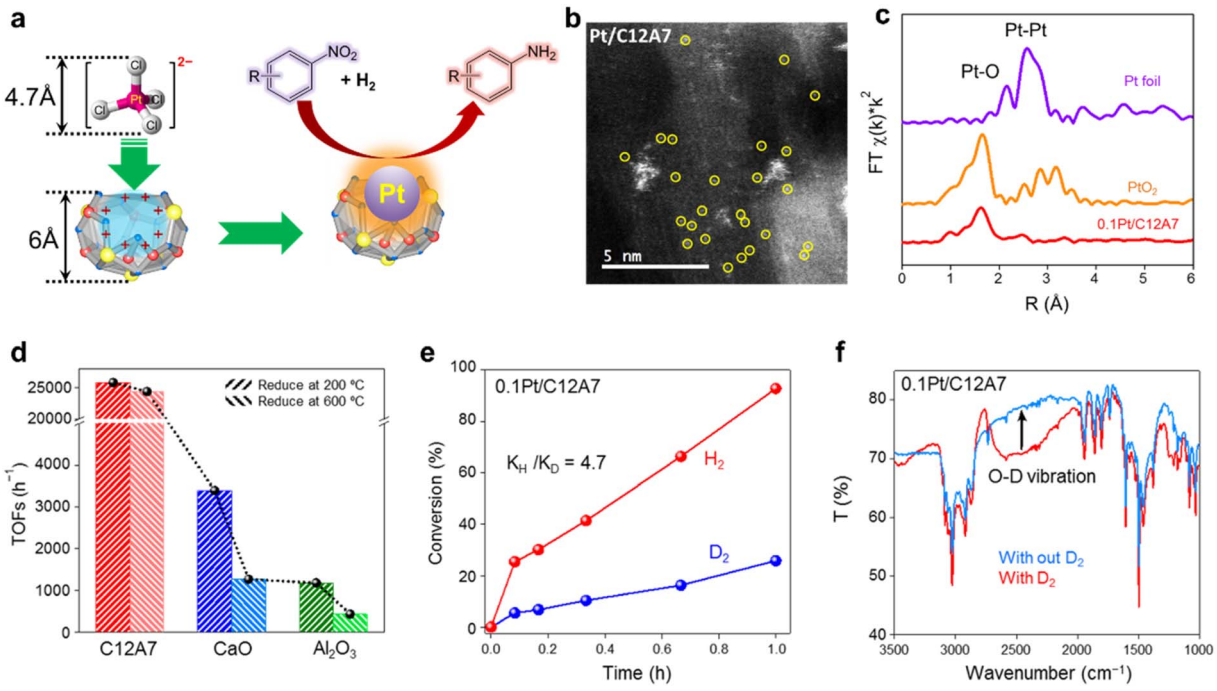

Fig. 26 (a) Schematic diagram of chemoselective hydrogenation of nitroarenes Pt single atom catalyst. (b) HAADF-STEM image of 0.1Pt/C12A7 single-atom structures. Single Pt atoms marked in yellow circles are uniformly dispersed on the C12A7 support. (c) Pt K-edge EXAFS spectra in the *R* space for 0.1Pt/C12A7. (d) Plot of 0.1Pt loaded on various supports at elevated reduction temperatures and their TOFs for the hydrogenation of 4-chloronitrobenzene. (e) Primary isotope effect observed on 0.1Pt/C12A7 for the hydrogenation of 4-chloronitrobenzene. (f) FTIR spectra for 0.1Pt/C12A7 after exposure to D_2 with the arrow pointing to the O–D vibration. This vibration disappears after the introduction of styrene. Copyright 2020, Springer Nature.

determining step (RDS) may involve the dissociation of O–H bonds instead of Pt–H bond cleavage over Pt/C12A7 (Fig. 26e). This is further confirmed by the FTIR results, in which the stretching vibration of O–D is only detected on Pt/C12A7 (Fig. 26f). Thus, such heterolytic cleavage of H_2 tend to generate $H^{\delta+}$ and $H^{\delta-}$ at the Pt–O interface of Pt/C12A7, which is favored for the selective hydrogenation of nitro groups.

2.4.2 Au^- ion stabilization. As described in Subsubsection 2.1.1, the irradiation of C12A7 with energetic inert gas ions, such as Ar^+, at high temperatures removes free O^{2-} ions from the lattice, leaving trapped electrons behind.[39] Miyakawa *et al.* implanted Au^+ ions into a single crystalline C12A7 at high temperatures, resulting in the formation of Au^- ions in C12A7 cages because of the comparable size of Au^- (0.366 nm) to the nanocage (Fig. 27a).[17] The implanted Au species are stabilized in the form of negative Au^- ions below the fluences of $\sim 1 \times 10^{16}$ cm^{-2} (Au volume concentration of $\sim 2 \times 10^{21}$ cm^{-3}). These ions are trapped in cages, which exhibit photoluminescence (PL) bands at 3.05 and 2.34 eV at temperatures below 150 K (Fig. 27b). The two emission bands can be attributed to intra ionic transitions of 6s6p ($^1P_1$, $^3P_2$, and $^3P_1$) to $^6S_2$ ($^1S_0$) with different energy levels (Fig. 27c). At the fluences above $\sim 3 \times 10^{16}$ cm^{-2}, the implanted Au ions aggregate to form nano-sized clusters, resulting in the quenching of PL bands. The appearance of a new absorption band at 2.43 eV is attributed to the surface plasmon of the free carriers of the cluster (Fig. 27d).

2.5. Other anion incorporation

2.5.1 NH^{2-}. Inorganic imide compounds, featuring abundant NH^{2-} groups, have been widely applied in hydrogen-related catalytic reactions owing to their high ratio of hydrogen amount and strong solid basicity.[117] However, the application of inorganic imide particles often suffers from poor stability under ambient conditions or in polar organic solvents. The C12A7 with a positively charged framework and an appropriate volume of nanocages is expected to stabilize NH^{2-}.

In 2014, Hayashi and co-workers developed an ammonothermal method to encapsulate NH^{2-} in C12A7 under the conditions of 35–55 MPa and 400–600 °C.[15] The concentration of the encapsulated NH^{2-} species is as high as 2.7×10^{20} cm^{-3}, and the obtained C12A7:NH^{2-} is chemically stable under ambient conditions. Such a large amount of encapsulated NH^{2-} with high stability makes C12A7:NH^{2-} a potential N1 source reagent for amination and amidation reactions. After that, Nakao *et al.* proposed a two-step mechanism of N_2 incorporation into the cages of C12A7 by modeling density functional theory (DFT).[118] It is reported that the decomposed NH^{2-} species from NH_3 is first incorporated into the surface cage structure of C12A7:e^-. Then, the as-captured NH^{2-} species react with each other to form N_2. Attention should be paid because such an encapsulation strategy of electroneutral N_2 molecules differs from the negatively charged species previously reported in C12A7.

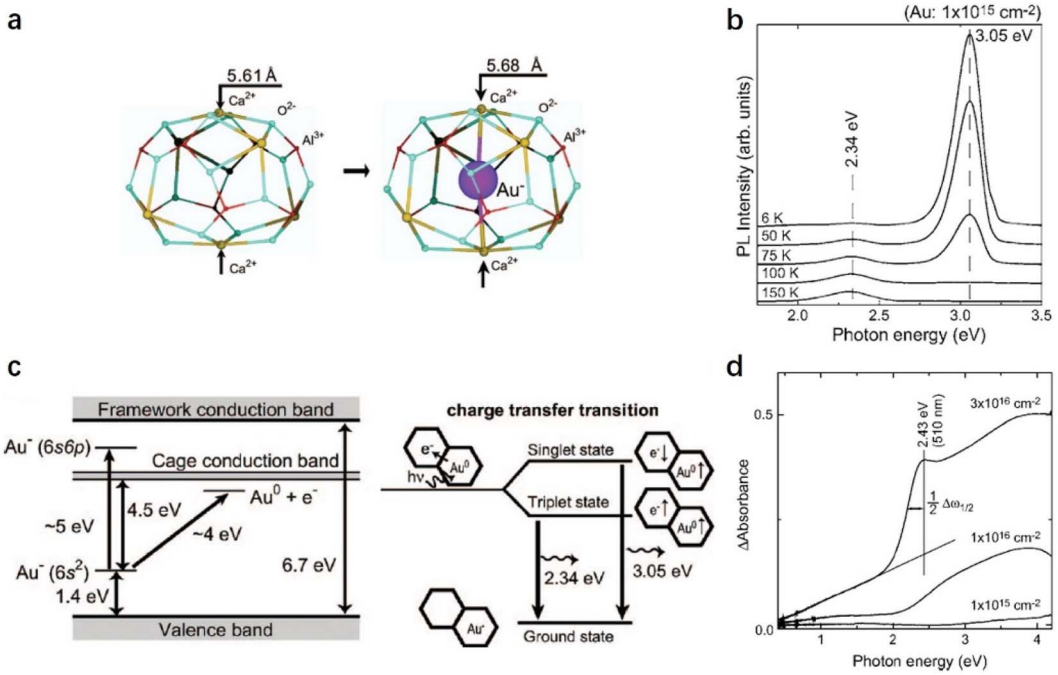

Fig. 27 (a) Local atomic structure of an Au^- ion-incorporated cage in C12A7 calculated using the two-cage QM cluster. (b) PL spectra of C12A7 single crystal implanted with Au^+ ions at a fluence of $\sim 10^{15}$ cm^{-2} at temperatures ranging from 6 to 150 K. (c) The left side shows energy levels of Au^- incorporated C12A7 calculated using the two-cage QM cluster. The right side shows a diagram of the charge transfer transition responsible for the photoluminescence, where the 3.05 and 2.34 eV bands are, respectively, assigned to the $Au^0 + e^- \rightarrow Au^-$ transitions from the singlet and triplet states to the ground state. (d) Differences in the optical absorption spectra of C12A7 crystals before and after Au^+ implantation at various fluences. Copyright 2006, American Physical Society.

2.5.2 Halogen ions. Owing to the termination at the surface of active metals, the presence of halogen species often leads to the poisoning of the metal catalyst.[119,120] However, halogen ions, such as Cl^- and F^-, with strong electron-withdrawing properties are also not beneficial in driving the catalytic reactions that require electrons, such as ammonia synthesis reaction.[121] Given the ion storage ability of the nanocage structure of C12A7, Li *et al.* reported that the C12A7 support could prevent the Cl^- poisoning of active metal Ru.[122] Consequently, Ru-loaded C12A7 was demonstrated to serve as an efficient catalyst with excellent Cl^- tolerance in ammonia synthesis. This contradicts conventional supported Ru catalysts in which MgO-supported Ru exhibits negligibly small activity when a tiny amount of Cl^- ions remains on the catalyst surface. They attributed the unique chlorine resistance of Ru-loaded C12A7 to the anion exchange properties of C12A7 because OH^- ions in the cages of C12A7 can be exchanged by Cl^- ions during the reaction.

Because of its strong etching ability, F^- ion is widely used in the fields of semiconductor etching, surface modifications, and so on.[123,124] The development of a suitable carrier, which can store F^- species stably and emit continuously, is highly demanded to promote the employment of F^- ion. In this context, Song *et al.* reported the preparation of the F^- storage emission material of C12A7–F^- through a solid-state reaction.[18] The concentration of the incorporated F^- of C12A7–F^- can reach $\sim 1.9 \times 10^{21}$ cm^{-3}, and the emission current density of F^- was as high as 16.7 ± 0.8 μA cm^{-2} at 800 °C under an extraction field of 1200 V cm^{-1}.

2.5.3 CN^-. The oxygen ions of the extra-framework of C12A7 can be substituted not only by single anions but also by polyanions. Recently, Schmidt *et al.* reported the preparation of C12A7–CN^- by a solid–gas reaction, in which stoichiometric CaO, α-Al_2O_3 and AlN were mixed and heated under vacuum at 1373 K, followed by an atmosphere change from air to nitrogen.[20] The reaction can be expressed by the following equation: $12CaO + 6Al_2O_3 + 2AlN + 2CO \rightarrow Ca_{12}Al_{14}O_{32}(CN)_2$. Carbon monoxide was formed *in situ* by the reaction of carbon in the furnace and carbon dioxide. The carbon dioxide was derived from the naturally formed $CaCO_3$ because the handling of CaO was performed in the air. The presence of the CN^- was proved using IR, ^{13}C-MAS-NMR and elemental analysis methods. By applying neutron diffraction studies, it is found that the orientation of the cyanide ions in the cages is slightly tilted to the 4 axis. After that, Schmidt *et al.* reported the C12A7–NO_2^- by partial oxidation of C12A7–CN^-.[125] Partial oxidation was achieved by heating C12A7–CN^- to 1083 K in the air for 4 h using a chamber furnace. The reaction can be expressed by the following equation: $Ca_{12}Al_{14}O_{32}(CN)_2 + 4O_2 \rightarrow Ca_{12}Al_{14}O_{32}(NO_2)_2 + 2CO_2$.

2.5.4 OH^-. OH^- in ionic oxide crystals has attracted considerable attention in the past decades.[106,126–129] It is reported that the defect sites of the ionic oxide are likely to be occupied by OH^- after UV irradiation in the presence of adsorbed hydrogen or water.[130] However, the concentration of irradiated OH^- anions is quite low.[128] The development of a new parent material that can store a high concentration of OH^- is highly required for the promotion of OH^- anion emissions. As we discussed in Subsubsection 2.2.1, when the C12A7–O^- was retreated at 1350 °C for 10 h under a mixture of Ar and H_2O atmosphere, the OH^- incorporated C12A7 can be obtained.[14,131] The concentration of OH^- anions can reach more than 7×10^{20} cm^{-3}, and OH^- anions are the dominating anions (90%) emitted from C12A7–OH^-.[14] The C12A7–OH^- material is expected to operate as an OH^- emitter for chemical synthesis, material modification, and sterilization.

3. Conclusion and perspectives

In this review, we summarized recent progress in the design and preparation of active anion-bearing C12A7 materials as catalysts and reagents in the fields of heterogeneous catalysis and important organic synthetic reactions. Owing to the versatility of C12A7 materials with various anion substitutions as well as their unique features (low work function/electron donation, metal–insulator transformation, and sub-nanometer-sized cage confinement), a series of C12A7-based functional materials have been designed and fabricated to satisfy specific catalytic and synthetic chemical processes. Important research contributions are highlighted to illustrate the manipulation of active anions (*e.g.*, e^-, O^-, O_2^-, H^- and metal single atom species) with enhanced performance owing to their potential chemical applications.

Although significant progress has been made, great challenges remain in the preparation and application of C12A7-based materials. (1) Owing to the necessity of employing harsh conditions to achieve active anion-bearing C12A7, the surface areas of these materials are limited to a few m^2 g^{-1}, which prevents further improvement of their catalytic performance. (2) It is always a conundrum to identify the interaction between the substituted active anions (especially the anions, such as O^-, O_2^-, H^-, NH^{2-} and OH^-) and loaded active metals, which restricts the purposed design and control synthesis of C12A7-based materials with desired active sites. (3) Although high performance has been achieved for C12A7-based materials, the exact reaction mechanism needs to be studied in depth to improve their functionality.

In a further study, the innovation of synthetic strategies and the fabrication of C12A7 with porous structure open new room for C12A7-based materials in chemical reactions. In addition, the employment of *in situ* characterization and tracer techniques would also be of great help in understanding both the active center structure and reaction mechanism to achieve a more rational material design. With rapid advances in synthetic and characteristic strategies of nanoscience and nanotechnology, the design and controlled synthesis of active anion-bearing C12A7 functional materials greatly contributes to sustainable development in the field of catalysis and organic synthesis.

Conflicts of interest

There are no conflicts to declare.

References

1 A. G. Slater and A. I. Cooper, *Science*, 2015, **348**, aaa8075.
2 X. Fan and Y. Jiao, in *Sustainable Nanoscale Engineering*, 2020, pp. 115–137.
3 R.-B. Lin, S. Xiang, W. Zhou and B. Chen, *Chem*, 2020, **6**, 337–363.
4 F. J. Maksoud, M. F. Velazquez de la Paz, A. J. Hann, J. Thanarak, G. C. Reilly, F. Claeyssens, N. H. Green and Y. S. Zhang, *J. Mater. Chem. B*, 2022, **10**, 8111–8165.
5 J. Prech, P. Pizarro, D. P. Serrano and J. Cejka, *Chem. Soc. Rev.*, 2018, **47**, 8263–8306.
6 G. Cai, P. Yan, L. Zhang, H. C. Zhou and H. L. Jiang, *Chem. Rev.*, 2021, **121**, 12278–12326.
7 W. Tian, H. Zhang, X. Duan, H. Sun, G. Shao and S. Wang, *Adv. Funct. Mater.*, 2020, **30**, 1909265.
8 Q. Zhang, S. Gao and J. Yu, *Chem. Rev.*, 2022, **123**, 6039–6106.
9 J. Jeevaratnam, L. S. D. Glasser and F. P. Glasser, *Nature*, 1962, **194**, 764–765.
10 S. Matsuishi, Y. Toda, M. Miyakawa, K. Hayashi, T. Kamiya, M. Hirano, I. Tanaka and H. Hosono, *Science*, 2003, **301**, 626–629.
11 K. Hayashi, S. Matsuishi, N. Ueda, M. Hirano and H. Hosono, *Chem. Mater.*, 2003, **15**, 1851–1854.
12 K. Hayashi, M. Hirano, S. Matsuishi and H. Hosono, *J. Am. Chem. Soc.*, 2002, **124**, 738–739.
13 K. Hayashi, *J. Solid State Chem.*, 2011, **184**, 1428–1432.
14 J. Li, F. Huang, L. Wang, S. Q. Yu, Y. Torimoto, M. Sadakata and Q. X. Li, *Chem. Mater.*, 2005, **17**, 2771–2774.
15 F. Hayashi, Y. Tomota, M. Kitano, Y. Toda, T. Yokoyama and H. Hosono, *J. Am. Chem. Soc.*, 2014, **136**, 11698–11706.
16 G. I. Zhmoidin and A. K. Chatterjee, *Cem. Concr. Res.*, 1984, **14**, 386–396.
17 M. Miyakawa, H. Kamioka, M. Hirano, T. Kamiya, P. V. Sushko, A. L. Shluger, N. Matsunami and H. Hosono, *Phys. Rev. B: Condens. Matter Mater. Phys.*, 2006, **73**, 205108.
18 C. Song, J. Sun, J. Li, S. Ning, M. Yamamoto, J. Tu, Y. Torimoto and Q. Li, *J. Phys. Chem. C*, 2008, **112**, 19061–19068.
19 J. Sun, C. Song, S. Ning, S. Lin and Q. Li, *Chin. J. Chem. Phys.*, 2009, **22**, 417–422.
20 A. Schmidt, M. Lerch, J.-P. Eufinger, J. Janek, R. Dolle, H.-D. Wiemh€ ofer, I. Tranca, M. M. Islam, T. Bredow, H. Boysen and M. Hoelzel, *Solid State Sci.*, 2014, **38**, 69–78.
21 M. Lacerda, J. T. S. Irvine, F. P. Glasser and A. R. West, *Nature*, 1988, **332**, 525–526.
22 H. Hosono, K. Hayashi, K. Kajihara, P. V. Sushko and A. L. Shluger, *Solid State Ionics*, 2009, **180**, 550–555.
23 A. Schmidt, M. Lerch, J. P. Eufinger, J. Janek, I. Trance, M. M. Islam, T. Bredow, R. Dolle, H. D. Wiemhöfer, H. Boysen and M. Hölzel, *Solid State Ionics*, 2014, **254**, 48–58.
24 J.-P. Eufinger, A. Schmidt, M. Lerch and J. Janek, *Phys. Chem. Chem. Phys.*, 2015, **17**, 6844–6857.
25 S. W. Kim, S. Matsuishi, T. Nomura, Y. Kubota, M. Takata, K. Hayashi, T. Kamiya, M. Hirano and H. Hosono, *Nano Lett.*, 2007, **7**, 1138–1143.
26 M. Miyakawa, S. W. Kim, M. Hirano, Y. Kohama, H. Kawaji, T. Atake, H. Ikegami, K. Kono and H. Hosono, *J. Am. Chem. Soc.*, 2007, **129**, 7270–7271.
27 Y. Kohama, S. W. Kim, T. Tojo, H. Kawaji, T. Atake, S. Matsuishi and H. Hosono, *Phys. Rev. B: Condens. Matter Mater. Phys.*, 2008, **77**, 092505.
28 S. W. Kim, M. Miyakawa, M. Hirano, Y. Kohama, H. Kawaji, T. Atake, H. Ikegami, K. Kono and H. Hosono, *Mater. Trans.*, 2008, **49**, 1748–1752.
29 S. Tanaka, T. Kato, A. Miyake, T. Kagayama, K. Shimizu, S. W. Kim, S. Matsuishi and H. Hosono, *J. Korean Phys. Soc.*, 2013, **63**, 477–480.
30 Y. Toda, S. W. Kim, K. Hayashi, M. Hirano, T. Kamiya, H. Hosono, T. Haraguchi and H. Yasuda, *Appl. Phys. Lett.*, 2005, **87**, 254103.
31 T. Kamiya, S. Aiba, M. Miyakawa, K. Nomura, S. Matsuishi, K. Hayashi, K. Ueda, M. Hirano and H. Hosono, *Chem. Mater.*, 2005, **17**, 6311–6316.
32 S. W. Kim, Y. Toda, K. Hayashi, M. Hirano and H. Hosono, *Chem. Mater.*, 2006, **18**, 1938–1944.
33 Y. Toda, S. Matsuishi, K. Hayashi, K. Ueda, T. Kamiya, M. Hirano and H. Hosono, *Adv. Mater.*, 2004, **16**, 685–689.
34 Q. X. Li, K. Hayashi, M. Nishioka, H. Kashiwagi, M. Hirano, Y. Torimoto, H. Hosono and M. Sadakata, *Appl. Phys. Lett.*, 2002, **80**, 4259–4261.
35 S. Matsuishi, K. Hayashi, M. Hirano and H. Hosono, *J. Am. Chem. Soc.*, 2005, **127**, 12454–12455.
36 T. N. Ye, Z. Xiao, J. Li, Y. Gong, H. Abe, Y. Niwa, M. Sasase, M. Kitano and H. Hosono, *Nat. Commun.*, 2020, **11**, 1020.
37 Y. Toda, H. Yanagi, E. Ikenaga, J. J. Kim, M. Kobata, S. Ueda, T. Kamiya, M. Hirano, K. Kobayashi and H. Hosono, *Adv. Mater.*, 2007, **19**, 3564–3569.
38 K. Hayashi, S. Matsuishi, T. Kamiya, M. Hirano and H. Hosono, *Nature*, 2002, **419**, 462–465.
39 M. Miyakawa, Y. Toda, K. Hayashi, M. Hirano, T. Kamiya, N. Matsunami and H. Hosono, *J. Appl. Phys.*, 2005, **97**, 023510.
40 S.-W. Kim, K. Hayashi, M. Hirano, H. Hosono and I. Tanaka, *J. Am. Ceram. Soc.*, 2006, **89**, 3294–3298.
41 S. Kim, M. Miyakawa, K. Hayashi, T. Sakai, M. Hirano and H. Hosono, *J. Am. Chem. Soc.*, 2005, **127**, 1370–1371.
42 S. Matsuishi, T. Nomura, M. Hirano, K. Kodama, S.-i. Shamoto and H. Hosono, *Chem. Mater.*, 2009, **21**, 2589–2591.
43 D. Jiang, Z. Zhao, S. Mu, H. Qian and J. Tong, *Inorg. Chem.*, 2019, **58**, 960–967.
44 F. Li, X. Zhang and J. Zhang, *Ceram. Int.*, 2019, **45**, 23830–23835.
45 Y. Xiao, X. Zhang and R. Li, *J. Am. Ceram. Soc.*, 2020, **104**, 1641–1648.
46 K. Kurashige, Y. Toda, S. Matstuishi, K. Hayashi, M. Hirano and H. Hosono, *Cryst. Growth Des.*, 2006, **6**, 1602–1605.
47 S. Gambarotta and J. Scott, *Angew. Chem., Int. Ed.*, 2004, **43**, 5298–5308.

48 S. Souma, T. Arakane, T. Sato, T. Takahashi, S. Wng Kim, S. Matsuishi and H. Hosono, *J. Phys. Soc. Jpn.*, 2010, **79**, 103704.
49 M. Kitano, Y. Inoue, Y. Yamazaki, F. Hayashi, S. Kanbara, S. Matsuishi, T. Yokoyama, S. W. Kim, M. Hara and H. Hosono, *Nat. Chem.*, 2012, **4**, 934–940.
50 S. Kanbara, M. Kitano, Y. Inoue, T. Yokoyama, M. Hara and H. Hosono, *J. Am. Chem. Soc.*, 2015, **137**, 14517–14524.
51 H. Hosono, *Catal. Lett.*, 2022, **152**, 307–314.
52 M. Kitano, S. Kanbara, Y. Inoue, N. Kuganathan, P. V. Sushko, T. Yokoyama, M. Hara and H. Hosono, *Nat. Commun.*, 2015, **6**, 6731.
53 Y. Inoue, M. Kitano, M. Tokunari, T. Taniguchi, K. Ooya, H. Abe, Y. Niwa, M. Sasase, M. Hara and H. Hosono, *ACS Catal.*, 2019, **9**, 1670–1679.
54 C. J. H. Jacobsen, S. Dahl, B. S. Clausen, S. Bahn, A. Logadottir and J. K. Nørskov, *J. Am. Chem. Soc.*, 2001, **123**, 8404–8405.
55 F. Hayashi, Y. Toda, Y. Kanie, M. Kitano, Y. Inoue, T. Yokoyama, M. Hara and H. Hosono, *Chem. Sci.*, 2013, **4**, 3124–3130.
56 P. Claus, A. Brückner, C. Mohr and H. Hofmeister, *J. Am. Chem. Soc.*, 2000, **122**, 11430–11439.
57 T. N. Ye, J. Li, M. Kitano, M. Sasase and H. Hosono, *Chem. Sci.*, 2016, **7**, 5969–5975.
58 H. Abe, Y. Niwa, M. Kitano, Y. Inoue, Y. Murakami, T. Yokoyama, M. Hara and H. Hosono, *J. Phys. Chem. C*, 2016, **120**, 8711–8716.
59 M. J. Sharif, M. Kitano, Y. Inoue, Y. Niwa, H. Abe, T. Yokoyama, M. Hara and H. Hosono, *J. Phys. Chem. C*, 2015, **119**, 11725–11731.
60 D. Widmann and R. J. Behm, *Acc. Chem. Res.*, 2014, **47**, 740–749.
61 B. Yoon, H. Hakkinen, U. Landman, A. S. Worz, J. M. Antonietti, S. Abbet, K. Judai and U. Heiz, *Science*, 2005, **307**, 403–407.
62 H. Öström, H. Öberg, H. Xin, J. LaRue, M. Beye, M. Dell'Angela, J. Gladh, M. L. Ng, J. A. Sellberg, S. Kaya, G. Mercurio, D. Nordlund, M. Hantschmann, F. Hieke, D. Kühn, W. F. Schlotter, G. L. Dakovski, J. J. Turner, M. P. Minitti, A. Mitra, S. P. Moeller, A. Föhlisch, M. Wolf, W. Wurth, M. Persson, J. K. Nørskov, F. Abild-Pedersen, H. Ogasawara, L. G. M. Pettersson and A. Nilsson, *Science*, 2015, **347**, 978–982.
63 G. C. Fu, *Acc. Chem. Res.*, 2008, **41**, 1555–1564.
64 B. Dai, Z. Li, M. Xu, J. Li, Y. Lu, J. Zai, L. Fan, S.-W. Park, M. Sasase, M. Kitano and H. Hosono, *J. Mater. Chem. A*, 2023, DOI: **10.1039/d2ta08899a**.
65 J. Li, B. Yin, T. Fuchigami, S. Inagi, H. Hosono and S. Ito, *Electrochem. Commun.*, 2012, **17**, 52–55.
66 J. Li, S. Inagi, T. Fuchigami, H. Hosono and S. Ito, *Electrochem. Commun.*, 2014, **44**, 45–48.
67 K. Khan, A. Khan Tareen, J. Li, U. Khan, A. Nairan, Y. Yuan, X. Zhang, M. Yang and Z. Ouyang, *Dalton Trans.*, 2018, **47**, 13498–13506.
68 Q. Hu, R. Tan, J. Li and W. Song, *J. Phys. Chem. Solids*, 2021, **149**, 109810.
69 H. Buchammagari, Y. Toda, M. Hirano, H. Hosono, D. Takeuchi and K. Osakada, *Org. Lett.*, 2007, **9**, 4287–4289.
70 S. M. Kim, H. S. Yoo, H. Hosono, J. W. Yang and S. W. Kim, *Sci. Rep.*, 2015, **5**, 10366.
71 Y. Toda, H. Hirayama, N. Kuganathan, A. Torrisi, P. V. Sushko and H. Hosono, *Nat. Commun.*, 2013, **4**, 2378.
72 J. H. Lunsford, *Adv. Catal.*, 1972, **22**, 265–344.
73 M. Che and A. Tench, *Adv. Catal.*, 1983, **32**, 1–148.
74 H. Hosono and Y. Abe, *Inorg. Chem.*, 1987, **26**, 1192–1195.
75 S. Yang, J. N. Kondo, K. Hayashi, M. Hirano, K. Domen and H. Hosono, *Chem. Mater.*, 2003, **16**, 104–110.
76 K. Hayashi, S. Matsuishi, M. Hirano and H. Hosono, *J. Phys. Chem. B*, 2004, **108**, 8920–8925.
77 S. Matsuishi, K. Hayashi, M. Hirano, I. Tanaka and H. Hosono, *J. Phys. Chem. B*, 2004, **108**, 18557–18568.
78 K. Hayashi, M. Hirano and H. Hosono, *Chem. Lett.*, 2005, **34**, 586–587.
79 A. T. Ashcroft, A. K. Cheetham, J. S. Foord, M. L. H. Green, C. P. Grey, A. J. Murrell and P. D. F. Vernon, *Nature*, 1990, **344**, 319–321.
80 P. D. F. Vernon, M. L. H. Green, A. K. Cheetham and A. T. Ashcroft, *Catal. Lett.*, 1990, **6**, 181–186.
81 P. D. F. Vernon, M. L. H. Green, A. K. Cheetham and A. T. Ashcroft, *Catal. Today*, 1992, **13**, 417–426.
82 L. Pino, A. Vita, M. Cordaro, V. Recupero and M. S. Hegde, *Appl. Catal., A*, 2003, **243**, 135–146.
83 S. Yang, J. N. Kondo, K. Hayashi, M. Hirano, K. Domen and H. Hosono, *Appl. Catal., A*, 2004, **277**, 239–246.
84 M. Steinberg, *Int. J. Hydrogen Energy*, 1989, **14**, 797–820.
85 B. McLellan, E. Shoko, A. Dicks and J. Dinizdacosta, *Int. J. Hydrogen Energy*, 2005, **30**, 669–679.
86 H. Pedersenmjaanes, L. Chan and E. Mastorakos, *Int. J. Hydrogen Energy*, 2005, **30**, 579–592.
87 D. Wang, S. Czernik and E. Chornet, *Energy Fuels*, 1998, **12**, 19–24.
88 L. a. Garcia, R. French, S. Czernik and E. Chornet, *Appl. Catal., A*, 2000, **201**, 225–239.
89 X. Zhu and R. Venderbosch, *Fuel*, 2005, **84**, 1007–1010.
90 Z. Wang, Y. Pan, T. Dong, X. Zhu, T. Kan, L. Yuan, Y. Torimoto, M. Sadakata and Q. Li, *Appl. Catal., A*, 2007, **320**, 24–34.
91 R. J. Schmidt, *Appl. Catal., A*, 2005, **280**, 89–103.
92 A. Reitzmann, E. Klemm and G. Emig, *Chem. Eng. J.*, 2002, **90**, 149–164.
93 T. Dong, J. Li, F. Huang, L. Wang, J. Tu, Y. Torimoto, M. Sadakata and Q. Li, *Chem. Commun.*, 2005, 2724–2726.
94 J. Pérez-Ramırez, F. Kapteijn, K. Schöffel and J. A. Moulijn, *Appl. Catal., B*, 2003, **44**, 117–151.
95 P. Pietrzyk, F. Zasada, W. Piskorz, A. Kotarba and Z. Sojka, *Catal. Today*, 2007, **119**, 219–227.
96 M. Ruszak, M. Inger, S. Witkowski, M. Wilk, A. Kotarba and Z. Sojka, *Catal. Lett.*, 2008, **126**, 72–77.
97 F. Witzel, G. A. Sill and W. K. Hall, *J. Catal.*, 1994, **149**, 229–237.
98 E. Fridell, H. Persson, L. Olsson, B. Westerberg, A. Amberntsson and M. Skoglundh, *Top. Catal.*, 2001, **16**, 133–137.

99 A. Amberntsson, M. Skoglundh, M. Jonsson and E. Fridell, *Catal. Today*, 2002, **73**, 279–286.
100 A. Gao, X. Zhu, H. Wang, J. Tu, P. Lin, Y. Torimoto, M. Sadakata and Q. Li, *J. Phys. Chem. B*, 2006, **110**, 11854–11862.
101 K. Hayashi, P. V. Sushko, Y. Hashimoto, A. L. Shluger and H. Hosono, *Nat. Commun.*, 2014, **5**, 3515.
102 M. Miyakawa, H. Murata and M. Imai, *Ceram. Int.*, 2019, **45**, 16028–16031.
103 C. J. Delbecq, B. Smaller and P. H. Yuster, *Phys. Rev.*, 1956, **104**, 599–604.
104 C. J. Delbecq and P. H. Yuster, *Phys. Rev.*, 1956, **104**, 605–606.
105 M. Chiesa, M. C. Paganini, E. Giamello, D. M. Murphy, C. Di Valentin and G. Pacchioni, *Acc. Chem. Res.*, 2006, **39**, 861–867.
106 D. Ricci, C. Di Valentin, G. Pacchioni, P. V. Sushko, A. L. Shluger and E. Giamello, *J. Am. Chem. Soc.*, 2003, **125**, 738–747.
107 J. Kammert, J. Moon, Y. Cheng, L. Deamen, S. Irle, V. Fung, J. Liu, K. Page, X. Ma, V. Phaneuf, J. Tong, A. J. Ramirez-Cuesta and Z. Wu, *J. Am. Chem. Soc.*, 2020, **142**, 7655–7667.
108 V. Sridharan, P. A. Suryavanshi and J. C. Menendez, *Chem. Rev.*, 2011, **111**, 7157–7259.
109 D. R. Aireddy and K. Ding, *ACS Catal.*, 2022, **12**, 4707–4723.
110 T.-N. Ye, J. Li, M. Kitano and H. Hosono, *Green Chem.*, 2017, **19**, 749–756.
111 B. Qiao, A. Wang, X. Yang, L. F. Allard, Z. Jiang, Y. Cui, J. Liu, J. Li and T. Zhang, *Nat. Chem.*, 2011, **3**, 634–641.
112 P. Liu, Y. Zhao, R. Qin, S. Mo, G. Chen, L. Gu, D. M. Chevrier, P. Zhang, Q. Guo, D. Zhang, B. Wu, G. Fu and N. Zheng, *Science*, 2016, **352**, 797–801.
113 N. Cheng, S. Stambula, D. Wang, M. N. Banis, J. Liu, A. Riese, B. Xiao, T.-K. Sham, L.-M. Liu, G. A. Botton and X. Sun, *Nat. Commun.*, 2016, **7**, 13638.
114 A. Wang, J. Li and T. Zhang, *Nat. Rev. Chem.*, 2018, **2**, 65–81.
115 X. F. Yang, A. Wang, B. Qiao, J. Li, J. Liu and T. Zhang, *Acc. Chem. Res.*, 2013, **46**, 1740–1748.
116 L. Nie, D. Mei, H. Xiong, B. Peng, Z. Ren, X. I. P. Hernandez, A. DeLaRiva, M. Wang, M. H. Engelhard, L. Kovarik, A. K. Datye and Y. Wang, *Science*, 2017, **358**, 1419–1423.
117 P. Chen, Z. Xiong, J. Luo, J. Lin and K. L. Tan, *Nature*, 2002, **420**, 302–304.
118 T. Nakao, K. Ogasawara, M. Kitano, S. Matsuishi, P. V. Sushko and H. Hosono, *J. Phys. Chem. Lett.*, 2021, **12**, 1295–1299.
119 M. V. Twigg and M. S. Spencer, *Appl. Catal., A*, 2001, **212**, 161–174.
120 M. Kurtz, H. Wilmer, T. Genger, O. Hinrichsen and M. Muhler, *Catal. Lett.*, 2003, **86**, 77–80.
121 S. Murata and K.-I. Aika, *Appl. Catal., A*, 1992, **82**, 1–12.
122 J. Li, M. Kitano, T.-N. Ye, M. Sasase, T. Yokoyama and H. Hosono, *ChemCatChem*, 2017, **9**, 3078–3083.
123 T. Shibayama, H. Shindo and Y. Horiike, *Plasma Sources Sci. Technol.*, 1996, **5**, 254–259.
124 C. M. S. Rauthan, G. S. Virdi, B. C. Pathak and A. Karthigeyan, *J. Appl. Phys.*, 1998, **83**, 3668–3677.
125 A. Schmidt, H. Boysen, A. Senyshyn and M. Lerch, *Z. Kristallogr. Cryst. Mater.*, 2014, **229**, 427–434.
126 B. Henderson and W. A. Sibley, *J. Chem. Phys.*, 1971, **55**, 1276–1285.
127 B. Henderson, J. L. Kolopus and W. P. Unruh, *J. Chem. Phys.*, 1971, **55**, 3519–3524.
128 H. Engstrom, J. B. Bates, J. C. Wang and M. M. Abraham, *Phys. Rev. B: Condens. Matter Mater. Phys.*, 1980, **21**, 1520–1526.
129 R. Ramírez, I. Colera, R. González, Y. Chen and M. R. Kokta, *Phys. Rev. B: Condens. Matter Mater. Phys.*, 2004, **69**, 014302.
130 E. Giamello, M. C. Paganini, D. M. Murphy, A. M. Ferrari and G. Pacchioni, *J. Phys. Chem. B*, 1997, **101**, 971–982.
131 V. K. Singh and F. P. Glasser, *Ceram. Int.*, 1988, **14**, 59–62.